Search for Charged Higgs Bosons Decaying to Top and Bottom Quarks in Proton-Antiproton Collisions

Gustavo Kertzscher

Master of Science

Department of Physics

McGill University
Montréal, Québec
July, 2008

A thesis submitted to McGill University in partial fulfilment of the requirements for the degree of Master of Science

ACKNOWLEDGEMENTS

I would like to thank my supervisor Prof. Brigitte Vachon for her constant support and guidance during the time of my M.Sc. studies. I would also like to thank Dr. Chris Potter for his guidance and for having initiated the research project that became the main focus of my graduate studies. Final results are presented in this thesis thanks to a concerted effort with Prof. Edward Boos, Viacheslav Bunichev, Dr. Lev Dudko, Dr. Potter and Prof. Vachon. Furthermore, I would like to thank Dr. Yann Coadou and Dag Gillberg for helping me understand the Single Top analysis package.

I would like to extend my gratitude to Dr. Cibran Santamarina-Rios and Andrew McCann for their careful reading of this thesis. Many thanks also go to Luis Valcarcel who helped me translating the English abstract into French.

ABSTRACT

The existence of a charged Higgs boson is hypothesised in different extensions of new physics beyond the Standard Model of particle physics. This thesis presents a search for charged Higgs bosons decaying to top and bottom quarks that was carried out using data collected by the DØ experiment at the Fermi National Accelerator Laboratory in Batavia, IL. The search investigated the existence of charged Higgs bosons in the mass range $180 \leq M_{H^+} \leq 300$ GeV/c^2, and in the context of different two-Higgs-doublet model extensions to the Standard Model. Nearly 1 fb^{-1} of data from proton-antiproton collisions at the centre-of-mass energy $\sqrt{s}$=1.96 TeV were analysed. No evidence for the existence of a charged Higgs boson was found. Upper limits on production cross-sections were derived for Types I, II, and III two-Higgs-doublet models. Excluded regions in the $(M_{H^+}, \tan\beta)$ plane for Type I were calculated.

ABRÉGÉ

L'existence d'un boson chargé de Higgs est suggérée hypothétiquement dans différentes extensions de la nouvelle physique allant au-delà du Modèle Standard de la physique des particules. Cette thèse présente une recherche de bosons chargés de Higgs se désintégrant en quarks top et bottom dans les données de l'expérience DØ au Fermi National Accelerator Laboratory à Batavia, IL. La fouille investigue l'existence de bosons chargés de Higgs ayant une masse $180 \leq M_{H^+} \leq 300$ GeV/c^2, et dans le contexte de différentes extensions du Modèle Standard à doublets de deux Higgs. Près de 1 fb^{-1} de données provenant de collisions proton-antiproton à une énergie de centre de masse $\sqrt{s}$=1.96 TeV ont été analysées. Aucune évidence de l'existence de bosons chargés n'a été trouvée. Des limites supérieures sur la section efficace de production ont été dérivées pour les Types I, II et III des modèles à doublets de deux Higgs. Des régions d'exclusion dans le plan $(M_{H^+}, \tan\beta)$ pour le Type I ont été calculées.

TABLE OF CONTENTS

LIST OF TABLES

LIST OF FIGURES

CHAPTER 1
Introduction

The smallest structures in nature are understood through studies of fundamental particles. On the theoretical side, the Standard Model provides a mathematical framework that explains observed particle properties and their interactions. Particle colliders and complex, large detectors are used in experimental approaches that study the way in which fundamental particles form, interact and decay.

To date, the Standard Model has been very successful in explaining results from particle physics experiments. Future experimental observations may be inconsistent with the Standard Model, possibly due to the following two facts: the theoretical mechanism which describes the generation of particle masses is ad-hoc, and the single physical observable produced by this mechanism, the electrically neutral Higgs boson, remains unseen.

If future experimental results will reveal that the Standard Model does not give a complete description of fundamental particles, an extension would be necessary to properly explain observations. One possible extension incorporates several Higgs bosons, of which two carry electric charge. Models with charged Higgs bosons deviate from the Standard Model Higgs mechanism, hence a charged Higgs boson discovery would require a modification of the description of fundamental particle physics.

This thesis presents a search for charged Higgs bosons decaying to top and bottom quarks. The search was undertaken at the Fermi National Accelerator Laboratory in Batavia, IL, in the United States of America. The results of proton-antiproton particle collisions delivered by the Tevatron collider were collected using the DØ detector. The data were examined and a search for charged Higgs bosons was performed. In particular Types I, II and III two-Higgs-doublet models (2HDMs) were explored in a charged Higgs boson mass range $180 \leq M_{H^+} \leq 300$ GeV/c^2. No discovery was made, however upper limits on the charged Higgs boson production cross-section were calculated. In addition, a small region of parameter space was excluded for the Type I 2HDM.

Chapter 2 gives the theoretical background for the Standard Model and the 2HDM. Chapter 3 introduces the Tevatron collider and the DØ detector. Chapter 4 gives a brief description of the data, background and signal samples used in this thesis. The selection of events that was used in the analysis is described in Chapter 5. The final analysis and results are presented in Chapter 6.

Specific contributions to this analysis by the author of this thesis are outlined here. Event selection requirements described in Chapter 5 were applied using a software package developed for the DØ single top analysis. Preselection and b tagging described in Sections 5.2 and 5.5, respectively, were applied on data, background sources and charged Higgs boson signal samples. Acceptances presented in Section 5.6 were derived for charged Higgs boson signal samples. Systematic uncertainties for jet energy scale and tag-rate functions presented in Section 5.7 were extracted for charged Higgs boson signal samples. Percent differences between exclusive charged Higgs boson signal samples described in Section 5.7 were calculated to validate the systematic uncertainty for the unknown proportion of initial state parton flavour pairs.

CHAPTER 2
Theory

2.1 The Standard Model

The Standard Model of particle physics describes three out of the four known fundamental forces of nature: the strong, weak and electromagnetic forces [1].[1] There exists two classes of elementary particles, namely half-integer spin particles, called fermions, and integer spin particles, called bosons. Fermions make up matter and are divided into quarks and leptons. Quarks are subject to all fundamental forces in the Standard Model. They carry either electric charge $+2/3\ e$ or $-1/3\ e$.[2] Leptons that are electrically neutral undergo the weak interaction while leptons that carry electric charge undergo weak and electromagnetic interactions. The electric charge of the leptons is either $0\ e$ or $-1\ e$. Table 2–1 lists the fermions, their masses and electric charges. Fermions are grouped into three generations.

Interactions between fermions occur through the exchange of gauge bosons. Fermions that are subject to the electromagnetic force exchange photons. The

---

[1] The fourth known fundamental force, gravity, is not included in the Standard Model. The strength of gravity is approximately in the order of 10^{-29} with respect to the weak force which is the weakest among Standard Model forces [2]. At the levels of energy reached thus far in laboratories, the force of gravity between elementary particles can be neglected due to its relative weakness compared to other forces.

[2] e is the unit charge, which is equivalent to the charge of a positive Hydrogen ion.

Table 2–1: Standard Model fermions, their masses and electric charges. The three fermion generations are shown.

Fermion flavours		mass (GeV/c^2)	electric charge (e)
1$^{\text{st}}$ Generation			
e	(electron)	5.11×10^{-4}	-1
ν_e	(electron neutrino)	$< 2 \times 10^{-9}$	0
d	(down quark)	3 to 7×10^{-3}	-1/3
u	(up quark)	1.5 to 3.5×10^{-3}	2/3
2$^{\text{nd}}$ Generation			
μ	(muon)	1.06×10^{-1}	-1
ν_μ	(muon neutrino)	$< 1.9 \times 10^{-4}$	0
s	(strange quark)	95×10^{-3}	-1/3
c	(charm quark)	1.25	2/3
3$^{\text{rd}}$ Generation			
τ	(tau)	1.78	-1
ν_τ	(tau neutrino)	$< 1.8 \times 10^{-2}$	0
b	(bottom quark)	4.2	-1/3
t	(top quark)	172.5 ± 2.7	2/3

$W^{\pm}$ and Z^0 bosons are exchanged between fermions undergoing a weak interaction. Fermions undergoing the strong interaction exchange gluons. Table 2–2 lists the gauge bosons, their masses, electric charges, and the force they mediate.

Each elementary particle in the Standard Model has an antiparticle (not explicitly shown in Table 2–1). An antiparticle has the same mass as its particle but with opposite electric charge and C-parity [2]. For instance, the antiparticle of the electron, called the positron, has a 0.511 MeV/c^2 mass but carries electric charge +1 e.

Colour charge is an internal degree of freedom for quarks and gluons, and can take three values (red, green and blue). Quarks form colour-singlet bound states, called hadrons, which are physical observables. Hadronic states have been observed in

Table 2–2: Gauge bosons for the strong, weak and electromagnetic (EM) forces. Also shown here are their masses and electric charges.

Mediators	mass (GeV/c^2)	force	electric charge (e)
photon	0	EM	0
$W^{\pm}$	80	weak	±1
Z^0	91	weak	0
gluon	0	strong	0

two and three valence quark combinations, called mesons and baryons, respectively. Quarks form colour-singlet bound states due to colour confinement which ensures that quarks in hadrons obey the Pauli exclusion principle [2]. Processes that form hadron states also occur when quarks are forced to separate [3]. The result is a spray of collimated colour-singlet particles, called a jet, moving in the direction of the original quark.

The proton is a baryon made of *uud* valence quarks that repeatedly interact with gluons. Gluons can subsequently undergo gluon splitting and form quark-antiquark pairs, called sea quarks [2]. Parton distribution functions describe the momentum fraction of a proton carried by different types of partons. Parton is the name for a single quark or gluon constituent.

The Standard Model electroweak theory unifies electromagnetic and weak interactions. The electroweak Lagrangian is both gauge invariant and symmetric under $SU(2)$ and $U(1)$ group transformations. Mass terms in quantum field theory, however, are not gauge invariant. An algebraic transformation, called electroweak symmetry breaking, circumvents this problem by introducing a complex scalar doublet and choosing a minima of the potential term such that

$$\langle\Phi\rangle_{\min} \;=\; \frac{1}{\sqrt{2}}\begin{pmatrix} 0 \\ v \end{pmatrix} \tag{2.1}$$

where Φ is the scalar doublet, and v is called the vacuum expectation value. Expanding the Lagrangian about the vacuum expectation value breaks the initial Lagrangian symmetry. The same procedure yields gauge invariant boson mass terms, and interaction terms between fermions and bosons. Electroweak symmetry breaking also leads to the existence of a neutral spin-0 scalar particle, the Higgs boson, which interacts with fermions and gauge bosons.

Charge conserving interactions between fermions and $W^{\pm}$ bosons define weak charged currents. In the lepton case, electrically charged antileptons and neutrinos belonging to the same generation interact with W^{+} bosons. In the quark case, up-type quarks and down-type antiquarks interact with W^{+} bosons.[3] Since there is a phase difference between mass eigenstates and weak force eigenstates, the mass eigenstate of each down-type quark (d, s, b) is expressed as a linear combination of their weak force eigenstates [4]. The Cabibbo-Kobayashi-Maskawa (CKM) transformation matrix relates weak force eigenstates to mass eigenstates of quarks. As a consequence, charged currents involving quarks do not strictly occur within the same

---

[3] Charge conjugate processes are defined in the same way: Antineutrinos and charged leptons interact with W^{-} bosons; down-type quarks and up-type antiquarks interact with W^{-} bosons. Charge conjugate states will be implied in the remainder of this thesis for brevity.

generation. The square of each CKM matrix element governs the mixing probability of quark flavours, hence also the cross-section of corresponding charged current processes. In the Standard Model, weak current interactions within each generation are strongly favoured.

2.2 Beyond the Standard Model

The Standard Model can explain observed particle behaviour with great precision, and it has predicted a wide range of phenomena. There are reasons that suggest the necessity to extend the Standard Model. For instance, the energy scale where gravity is expected to be dominant ($\mathcal{O}(10^{16})$ GeV), has not been probed experimentally. There is therefore no guarantee for the Standard Model to hold at these energy scales that are much higher than the mass scale of known non-composite particles (up to $\mathcal{O}(10^{2})$ GeV/c^2). Models beyond the Standard Model are called for also from the fact that gravity has not been unified with the other known fundamental forces.

A discovery of the Higgs boson would provide strong support for the Standard Model mass generating mechanism. The Higgs boson has not yet been discovered, which motivates extended models to the Standard Model. Furthermore, there is no obvious reason to settle for a model with one single Higgs doublet. Different extensions to the Standard Model rely on mass generating mechanisms with two Higgs doublets. Such models generate multiple physical Higgs bosons, including charge carrying ones. The rest of this thesis will be devoted to exploring charged Higgs bosons.

2.3 The Two-Higgs-Doublet Model

Two $SU(2)$ doublet scalar fields are incorporated in the minimal extension of the Standard Model Higgs sector [5]. In this model, called the two-Higgs-doublet model (2HDM), electroweak symmetry breaking can occur by choosing

$$\langle\Phi_1\rangle_{min} = \begin{pmatrix} 0 \\ v_1 \end{pmatrix}, \quad \langle\Phi_2\rangle_{min} = \begin{pmatrix} 0 \\ v_2 \end{pmatrix} \tag{2.2}$$

as the minimum of the potential of the scalar fields Φ_1 and Φ_2. The ratio of the vacuum expectation values is defined as $\tan\beta = v_2/v_1$. Electroweak symmetry breaking generates five physical spin-0 scalar particles, or Higgs bosons. Three Higgs bosons are electrically neutral, H^0, h^0 and A^0, and two carry electric charge, H^+ and H^-.[4] Charged Higgs bosons are different from any of the Standard Model particles. The ways in which charged Higgs bosons couple with fermions differ from Standard Model Higgs boson couplings with fermions.

Quark couplings with charged Higgs bosons can be described by the general Lagrangian

$$\mathcal{L} = \frac{1}{2}H^+\bar{q}_i\left[c_L^{ij}\left(1-\gamma^5\right) + c_R^{ij}\left(1+\gamma^5\right)\right]q_j + \text{h.c.} \tag{2.3}$$

where i represents the down-type antiquark flavour, and j represents the up-type quark flavour. The symbols H^+, $\bar{q}_i$ and q_j represent the fields of the charged Higgs

---

[4] In the remainder of this thesis, the H^+ notation will be used to refer to both H^+ and H^- states.

boson, antiquark and quark, respectively. The symbols c_L^{ij} and c_R^{ij} represent the coupling between the charged Higgs boson and a left-handed (L) or right-handed (R) spinor projection of the quark field, respectively. The fermion fields are projected into left-handed or right-handed Dirac spinor components using the chiral operator $(1-\gamma^5)/2$ or $(1+\gamma^5)/2$, where γ^5 is defined as the product of Dirac γ matrices $\gamma^5 = i\gamma^0\gamma^1\gamma^2\gamma^3$. Chiral symmetry is a conserved property in weak interactions.

The 2HDM is divided into different types depending on the strategy used to avoid flavour changing neutral currents [6]. Flavour changing neutral currents are suppressed in the Standard Model.[5] The difference between 2HDM types is in how left-handed (c_L^{ij}) and right-handed (c_R^{ij}) couplings are structured. Three model types will be discussed here.

- **Type I** One Higgs doublet couples to quarks, while the other doublet does not [5]. The couplings between charged Higgs bosons and quarks are defined as [7]

$$c_L^{ij} = -V_{\mathrm{CKM}}^{ij} \frac{g_w m_i}{\sqrt{2} M_W} \tan\beta \tag{2.4}$$

$$c_R^{ij} = V_{\mathrm{CKM}}^{ij} \frac{g_w m_j}{\sqrt{2} M_W} \tan\beta \tag{2.5}$$

  where V_{CKM}^{ij} represents the CKM transformation matrix element appropriate to the ij flavours. The symbol g_w is the weak coupling constant. Symbols m_i

---

[5] An example of a flavour changing neutral current is the decay $K^0 \rightarrow \mu^+\mu^-$, where the initial state flavour composition ($d\bar{s}$ or $s\bar{d}$) is not the same as in the final state. The decay process represents a neutral current since the net charge in initial and final states is zero.

and m_j represent the masses of interacting quarks and M_W, that of the W^+ boson.

- **Type II** One Higgs doublet couples to up-type quarks, while the other doublet couples to down-type quarks [5]. The couplings between charged Higgs bosons and quarks are defined as [7]

$$c_L^{ij} = V_{\text{CKM}}^{ij} \frac{g_w m_i}{\sqrt{2} M_W} \cot\beta \tag{2.6}$$

$$c_R^{ij} = V_{\text{CKM}}^{ij} \frac{g_w m_j}{\sqrt{2} M_W} \tan\beta \tag{2.7}$$

- **Type III** This model is defined in a basis where only one of the Higgs doublet has a non-zero vacuum expectation value [8]. Both doublets couple to quarks, and the couplings are defined as

$$c_L^{ij} = -(V_{\text{CKM}} \hat{Y})_{ij} \tag{2.8}$$

$$c_R^{ij} = (\hat{Y}^\dagger V_{\text{CKM}})_{ij} \tag{2.9}$$

where $\hat{Y}$ is a matrix with elements that follow the ansatz $\hat{Y}_{ij} = \xi_{ij}\sqrt{2m_i m_j}/v$. The symbol ξ_{ij} represents the free parameters in the Type III 2HDM which are expected to be near unity [6, 8]. The symbol v represents the vacuum expectation value of one of the Higgs doublet fields. The flavour changing neutral currents are suppressed by the definition of the mixing matrix $\hat{Y}$ due to the small mass of quarks in the first and second generations [9]. The analysis presented in this thesis simplifies $\hat{Y}$ by considering $\xi_{ij} = \xi$ which implies that all possible free parameters have the same value.

Fermion couplings for Type I and II 2HDMs are directly proportional to fermion masses and the $\tan\beta$ parameter. In the Type III model, the couplings are directly proportional to fermion masses, but there is no $\tan\beta$ dependency since this parameter is not defined. All 2HDM couplings between quarks and charged Higgs bosons are governed by the CKM transformation matrix, hence processes that conserve generation numbers are favoured.

2.3.1 Charged Higgs Boson Production Cross-Section

The charged Higgs boson production cross-section through proton-antiproton collisions is defined as

$$\sigma(p\bar{p} \to H^+) = \sum_{qq'} \int dx f_q(x) f_{q'}(M_{H^+}/sx) \frac{\pi}{M_{H^+} sx} \text{ avg} \sum_s |\mathcal{M}|^2 \tag{2.10}$$

where q and q' are the initial state parton flavours, x is the fraction of beam momentum carried by the partons, f_q and $f_{q'}$ are the parton distribution functions for initial state parton flavours, M_{H^+} is the mass of the charged Higgs boson, s is the square of the collider centre-of-mass energy in the collision, and $\text{avg} \sum_s |\mathcal{M}|^2$ is the spin-averaged square of the scattering amplitude [7]. The scattering amplitude is directly proportional to the couplings between charged Higgs bosons and initial state partons. The production cross-section is therefore model dependent according to Equations 2.4 to 2.9.

Figure 2–1 shows the predicted charged Higgs boson production cross-section in proton-antiproton collisions for Types I, II and III 2HDMs. Sizeable cross-sections can be expected in present day particle colliders, for some models and values of parameters.

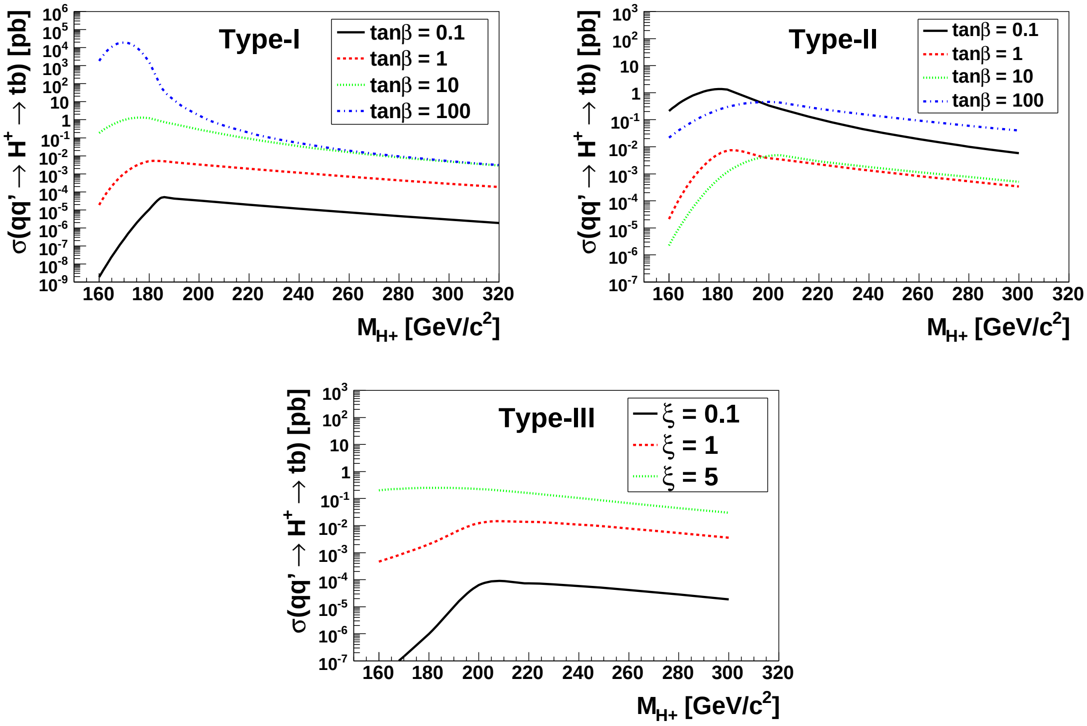

Figure 2–1: Production cross-sections of the charged Higgs boson times the branching ratio of the top and bottom quark final state, for Types I, II and III 2HDMs [10]. These cross-section times branching ratio values were calculated using the CompHEP Monte Carlo generator [11] and are shown here for different values of the $\tan\beta$ parameter (Types I and II) or the ξ mixing parameter (Type III).

2.3.2 Charged Higgs Boson Width

The total width of a charged Higgs boson is defined by the Golden Rule for Decays [2]. The total width is the sum of partial widths, where the latter is equal to the integral of the scattering amplitude squared of the decay process times the available phase space. A model dependency is introduced from the proportionality of the partial width to the scattering amplitude squared, which is proportional to the couplings in Equations 2.4 to 2.9. Figure 2–2 shows the total width of a charged Higgs boson for Types I, II and III 2HDMs. The total width is large for particular values of model parameters, depending on the 2HDM type. In some cases the total width can be larger than the experimental resolution, as will be described in Section 6.2.

2.3.3 Branching Ratios

Branching ratios for different decay processes are given by the ratio of the partial width of a process to the total width [4]. The branching ratio is large if the coupling of a process is large, due to the direct proportionality between branching ratios and partial widths. Given the 2HDM couplings presented in Equations 2.4 to 2.9, the charged Higgs boson decays primarily into particles with large mass. Figure 2–3 illustrates how the branching ratio is affected by the mass of the final state particles for two charged Higgs masses greater than the sum of top and bottom quark masses. In all 2HDM types, the branching ratio of the top and bottom quark decay mode dominates in most regions of the parameter space. This final state is therefore important in searches for heavy charged Higgs bosons. The branching ratio of the charm and strange quark final state is prominent in decays of charged Higgs bosons with masses smaller than the top quark. In decays of charged Higgs bosons with masses greater than the top quark, the charm and strange quark final state is highly suppressed. The suppression of the charm and strange quark final state is due to the fact that fermion couplings with charged Higgs bosons are proportional to the fermion masses and since the combined charm and strange quark mass is much smaller than the combined top and bottom quark mass.

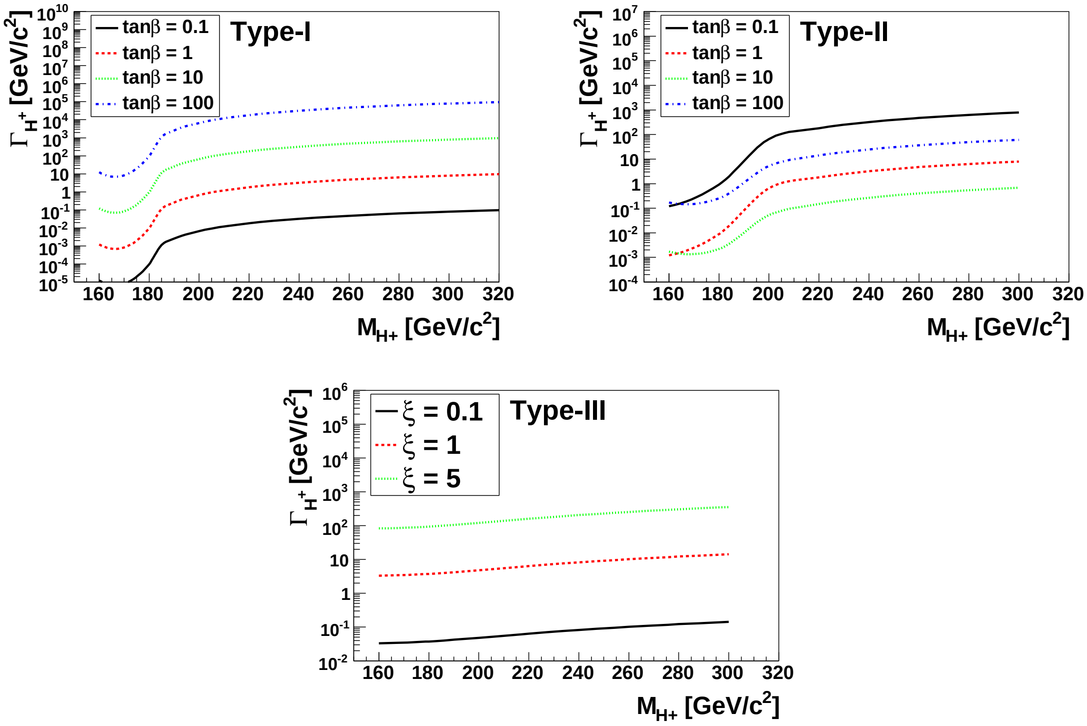

Figure 2–2: The total width of a charged Higgs boson (Γ_{H^+}) for Types I, II and III 2HDMs [10]. Widths are shown here for different values of the charged Higgs mass, and the parameters $\tan\beta$ (Types I and II) or ξ (Type III). The widths were calculated using the CompHEP Monte Carlo generator, assuming that charged Higgs bosons decay to fermions only. This assumption was based on the fact that charged Higgs decays to fermions with a greater than 90% branching ratio for $200 < M_{H^+} < 300$ and $1 < \tan\beta < 100$ for the Type II 2HDM (see Section 2.3.3) and a greater than 55% branching ratio for $200 < M_{H^+} < 300$ for the Type III 2HDM [8]. The fact that only fermion final states were considered when calculating the total width resulted in an underestimation. The calculated total widths were used to estimate the experimental resolution (see Section 6.2). The calculated total width for the Type II 2HDM with parameter values $M_{H^+} = 200$ and $\tan\beta = 1$ was used to extract the experimental resolution. Since the branching ratio is near unity for these parameter values, the underestimation is negligible and did not significantly affect the calculation of the experimental resolution.

2.3.4 Existing Constraints

Constraints on the production cross-section of charged Higgs bosons have been determined from direct and indirect searches [1]. Constraints from direct searches were extracted from experiments at the CERN electron-positron collider (LEP) [13, 14, 15, 16], and at the Tevatron [17, 18, 19]. The LEP experiments searched for charged Higgs boson pairs produced in photon or Z^0 boson decays [20, 21]. Assuming the Type II 2HDM, a lower charged Higgs mass bound of $M_{H^\pm} > 78.6$ GeV/c^2 was extracted at the 95% confidence level [1]. Tevatron experiments search for processes where the top quark decays into a bottom quark and the charged Higgs boson, hence in the mass range below the mass of the top quark. The Tevatron CDF experiment excluded the mass range $80 \leq M_{H^+} \leq 160$ GeV/c^2, in the parameter regions $\tan\beta < 1$ and $\tan\beta > 30$, under minimal supersymmetry model assumptions that are stated in [19]. Figure 2–4 shows the excluded regions for charged Higgs boson production determined from direct searches.

Indirect searches have also been undertaken at B factories [22].[6] These searches are sensitive to the presence of charged Higgs bosons in $b \to s\gamma$ loop processes. The charged Higgs mass has been constrained to $M_{H^+} > 295$ GeV/c^2, under Type II 2HDM assumptions. Indirect searches assume no contribution from other new particles and are therefore more model dependent.

---

[6] A B factory is a particle collider that collides electrons and positrons at a particular resonance energy, with large probability of producing b-quark mesons.

No direct search has ruled out the existence of a charged Higgs boson with the mass greater than the mass of the top quark. This search explores large mass ranges and is complementary to previous searches.

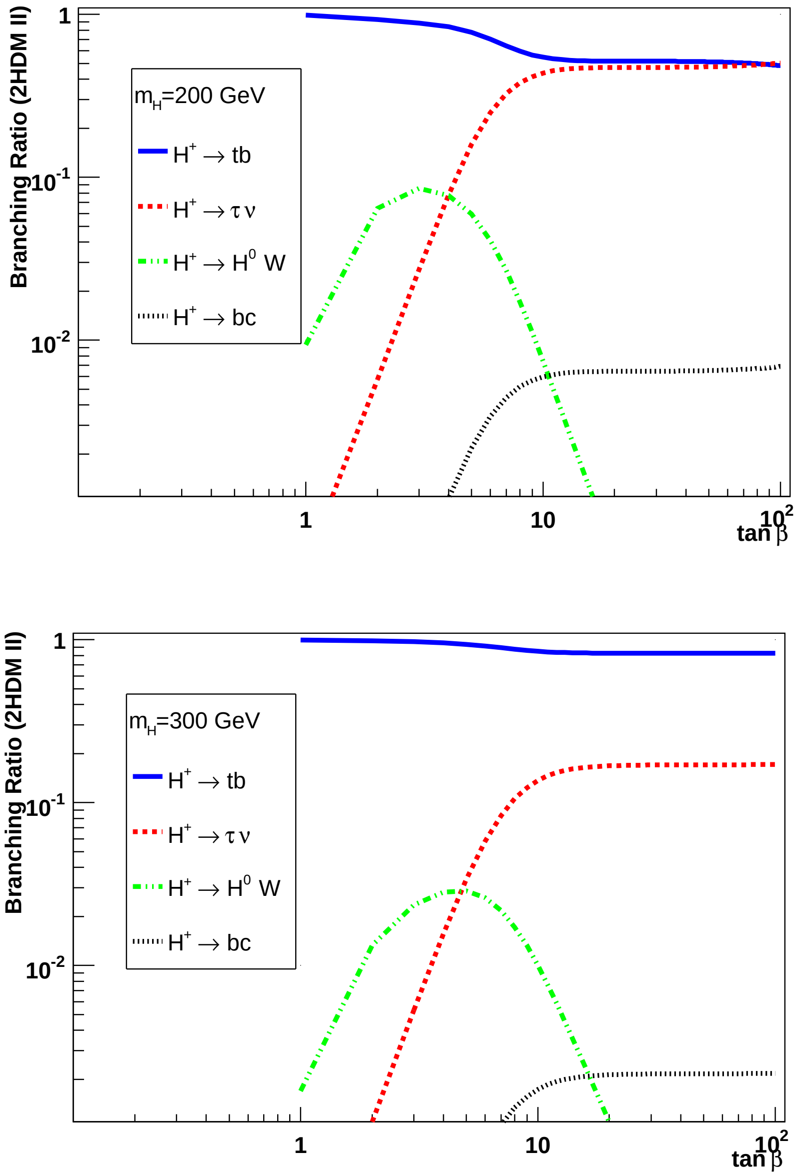

Figure 2–3: Branching ratios of the charged Higgs boson in the Type II 2HDM, calculated as functions of $\tan\beta$ for mass cases $M_{H^+} = 200$ GeV/c^2 (top) and $M_{H^+} = 300$ GeV/c^2 (below) [10]. These branching ratios were calculated using HDECAY [12].

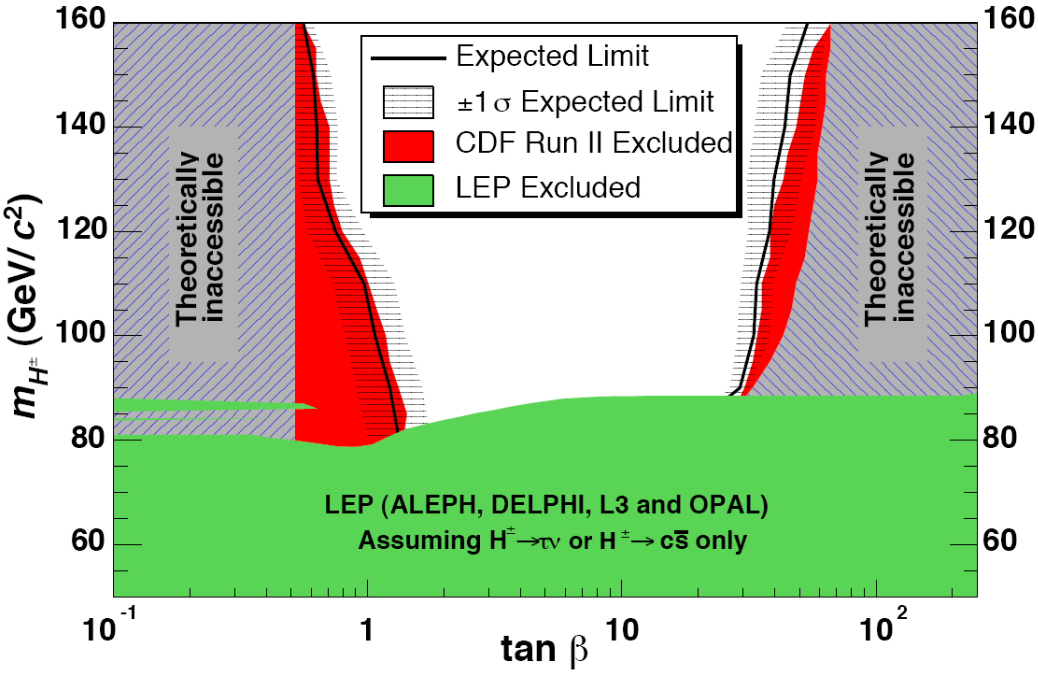

Figure 2–4: Charged Higgs boson excluded regions in the $(M_{H^+}, \tan\beta)$ plane at the 95% confidence level [1]. The LEP searches assumed that the $H^+ \to c\bar{s}$ and $H^+ \to \tau^+\nu$ modes exhausted the possible final states. The Tevatron experiments searched for charged Higgs produced in the $t \to \bar{b}H^+$ process, assuming charged Higgs coupling only with $\tau\nu$, cs, t^*b or Wh^0.

CHAPTER 3
Experimental Environment

This chapter gives a summary of the technology that was used in the Tevatron collider and the DØ experiment. A brief description of the accelerator chains for protons and antiprotons is given in Section 3.1. The DØ detector components are described in Section 3.2.

3.1 The Tevatron Collider

The Tevatron collider [23] is located at the Fermi National Accelerator Laboratory (Fermilab) in Batavia, IL, USA. The circular collider is 2 km in diameter and collides protons with counter-rotating antiprotons at a 1.96 TeV centre-of-mass energy. The Run II data taking period started in June 2001 and is due to finish at the end of 2009. Figure 3.1 shows a schematic view of the Tevatron collider chain.

Proton production involves three accelerators: the pre-accelerator, Linac and Booster. The pre-accelerator is based on a Cockcroft-Walton design. Negatively charged Hydrogen ions are contained in an electrically charged dome fixed at a -750 keV potential. The ions are accelerated towards a grounded wall into an energy of 750 keV. These ions are transferred into the Linac which uses radio frequency cavities to accelerate the Hydrogen ion beam to an energy of 400 MeV. The ion beam strikes a thin layer of carbon foil that strips away the electrons, leaving behind bare protons. These protons eventually enter the Booster which is a 75 m

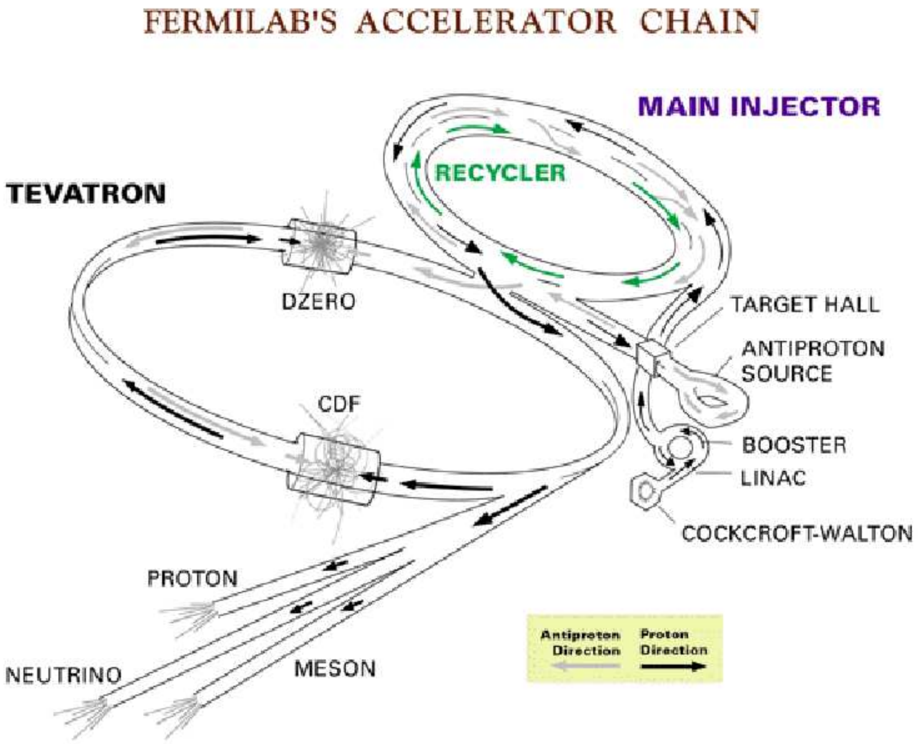

Figure 3–1: Schematic view of the Tevatron collider chain [24].

radius synchrotron. The Booster accelerates the protons to the extraction energy of 8 GeV.

Antiproton ($\bar{p}$) production begins with the Main Injector. The Main injector accepts protons (p) from the Booster and accelerates them to an energy of 120 GeV. These protons are subsequently directed towards the Target Hall where they hit a nickel target and undergo the reaction $p + p \rightarrow \bar{p} + p + p + p$. Carrying a momentum that peaks at an energy of 8 GeV, the secondary antiprotons are transferred into the Debuncher synchrotron (located inside the tunnel labelled "Antiproton Source" in Figure 3.1). The Debuncher uses radio frequency cavities and stochastic cooling techniques to reduce the antiproton beam size and the momentum spread [23].

The Accumulator, located inside the same tunnel as the Main Injector, acts as a storage ring for antiprotons. Antiprotons from the Debuncher are injected into the accumulator which performs additional stochastic cooling until the beam reaches the desired intensity. The antiproton beam gets transferred into the Recycler for storage and for further cooling at a constant energy of 8 GeV.

The Main Injector receives protons and antiprotons from the Booster and Recycler, respectively, and accelerates them from an energy of 8 GeV to 150 GeV. Proton and antiproton bunches are eventually transferred into the Tevatron until it contains 36 bunches of each type. The Tevatron uses cryogenically cooled superconducting magnets to accelerate the proton and antiproton bunches into an energy of 980 GeV. At this energy, the protons and antiprotons are brought into collision at a centre-of-mass energy of 1.96 TeV. Collisions take place at two interaction points in the Tevatron, where the DØ and CDF detectors are located. Data recorded by the DØ detector is analysed in this thesis.

The result of collisions are recorded in a period lasting approximately 20 hours until the instantaneous luminosity has decreased by approximately one order of magnitude. The integrated luminosity, $\mathcal{L}$, is a measurement of the number of collisions delivered from the Tevatron, and is measured in units of inverse barns (b^{-1}).[1] The

---

[1] 1 b^{-1} is equivalent to 10^{28} m^{-2}. The instantaneous luminosity is measured in units of $\mathrm{b}^{-1}\mathrm{s}^{-1}$.

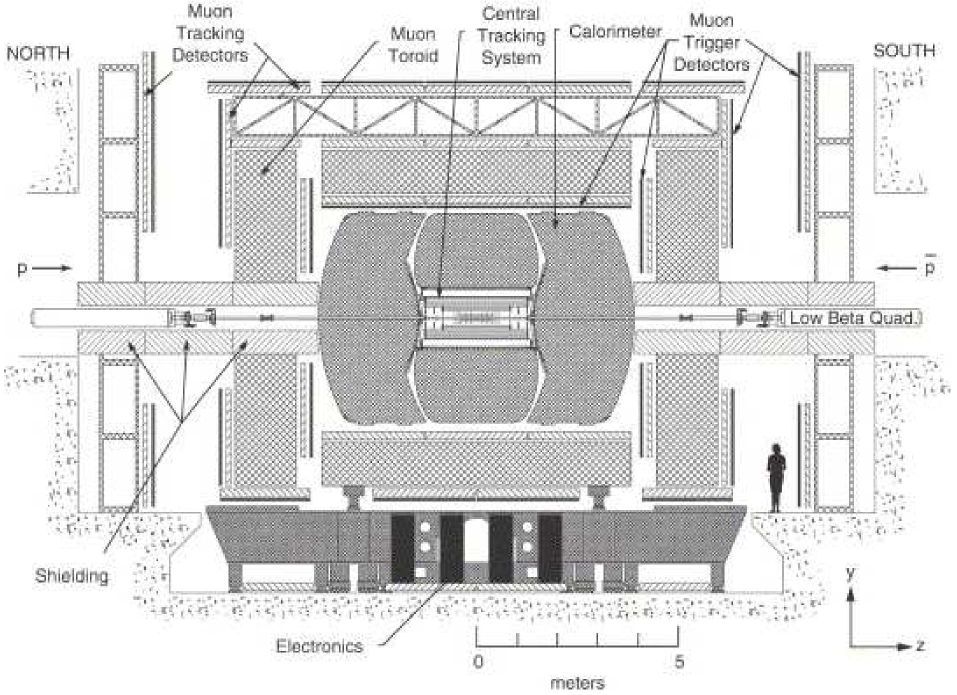

Figure 3–2: Sideview of the DØ detector for Run II [24].

total number of recorded events of a particular type, N, is equal to

$$N = \mathcal{L}\sigma\epsilon \tag{3.1}$$

where σ is the cross-section of a process (measured in units of barns), and ϵ is the efficiency for identifying the events of interest.

3.2 The DØ Detector

The upgraded DØ detector [24] for Run II was designed to record the result of a wide range of physics phenomena. As shown in Figure 3.2, the DØ detector comprises three subsystems: the central tracking system, calorimeter and muon spectrometer. Protons enter the north side of the detector region and travel in the positive z-axis direction. Antiprotons travel in the opposite direction. The r coordinate defines the radial distance from the z-axis. The θ and ϕ angles define polar and azimuthal angles, respectively. The pseudorapidity is defined as $\eta = -\ln[\tan(\theta/2)]$. Pseudorapidity approximates the Lorentz invariant rapidity, $y = 1/2 \ln[(E + p_z c)/(E - p_z c)]$, for particles that approach the limit $(mc^2/E) \rightarrow 0$.

3.2.1 Central Tracking System

The central tracking system is the innermost detector sub-system and it provides precise measurements of charged particle trajectories and momenta. Particle trajectories are measured using silicon microstrip detectors and a surrounding scintillating fibre detector. Outside this system is a superconducting solenoidal magnet which allows for momentum measurements. The magnet induces an almost uniform 2 T central magnetic field parallel to the z-axis. The presence of a magnetic field curves the trajectory of charged particles. The measurements of the trajectory's curvature and a mass assumption are used to infer the momentum of charged particles. The central tracking system measures primary vertex interactions to a 35 μm resolution along the z-direction. The resolution in the $r - \phi$ plane is 15 μm for particles with $|\eta| = 0$ and transverse momentum greater than 10 GeV/c.

Silicon Microstrip Tracker. The silicon microstrip tracker provides precise measurements of charged particle trajectories near the initial interaction point [24]. The silicon microstrip tracker is the sub-detector closest to the proton-antiproton interaction and provides trajectory measurements in the pseudorapidity region $|\eta| < 3$. The silicon detectors are arranged in disks and barrels that are perpendicular and parallel, respectively, to the beam axis. The arrangement was motivated by the

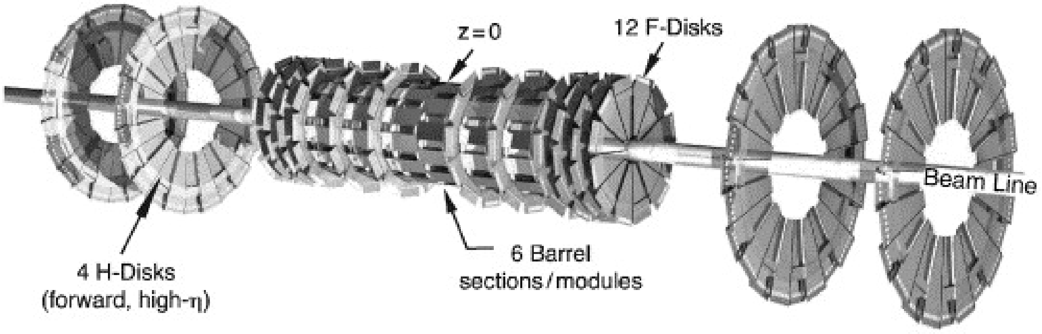

Figure 3–3: Schematic diagram of the silicon microstrip tracker disk and barrel modules [24].

length of the interaction region[2] and the expected particle pseudorapidity distributions. The central disk and barrel modules are necessary for $r-\phi$ measurements of particles with small pseudorapidity ($|\eta| \lesssim 1.5$). Disks at the far ends provide precise $r-z$ and $r-\phi$ measurements for particles with larger pseudorapidity ($1.5 \lesssim |\eta| < 3$). All modules use a combination of silicon based sensors with a pitch[3] ranging from 40 to 153 μm. Sensors located in the barrel region are primarily of a double-sided architecture where axial sensor strips are off-set by a 2° angle. This arrangement provides a two dimensional hit information. Figure 3–3 shows a diagram of the silicon microstrip tracker.

Central Fibre Tracker. The central fibre tracker complements the silicon microstrip tracker by sampling a larger region along charged particle trajectories.

---

[2] The length of the interaction region has an approximate root-mean-square value of 25 cm along the beam direction.

[3] The pitch is the distance between the centres of two adjacent sensor regions. For the silicon microstrip tracker, these are strips.

Fibres consist of a scintillating material that emits light due to traversing charged particles. The scintillation light is transferred to a fluorescent dye which is mixed with the scintillating material of the fibres. The advantage of the fluorescence light is the fast fluorescence decay, however the mean free path of the fluorescence light in the fibre is only a few hundred microns. The fibre material is therefore doped with a wavelength shifting dye. This dye absorbs the fluorescence light and re-emits light with a wavelength that gets better transmitted in the fibre. Waveguides transport the wavelength shifted light to visible light photon counters for readout outside the detector.

Figure 3–4 shows the geometry of the central fibre tracker. Fibres are attached on supporting cylinders that provide pseudorapidity coverage $\eta < 1.7$. Each cylinder supports two layers of fibres that are off-set by a 3° angle to provide two dimensional hit information. The resolution of one doublet layer of fibres is approximately 100 μm, if the individual $r - \phi$ fibre position is known to at least 50 μm.

3.2.2 Calorimeter

Calorimeters are designed to measure particle energies. The DØ calorimeter [25, 24] is a sampling calorimeter that consists of alternating layers of inactive material and instrumented regions. Particles traversing inactive regions lose energy through mainly electromagnetic and hadronic interactions.[4] The energy is lost mainly in the inactive region, which consists of electrically grounded absorber plates made

---

[4] Electrons and photons lose their energy mainly through bremsstrahlung while hadrons lose energy through strong and nuclear processes.

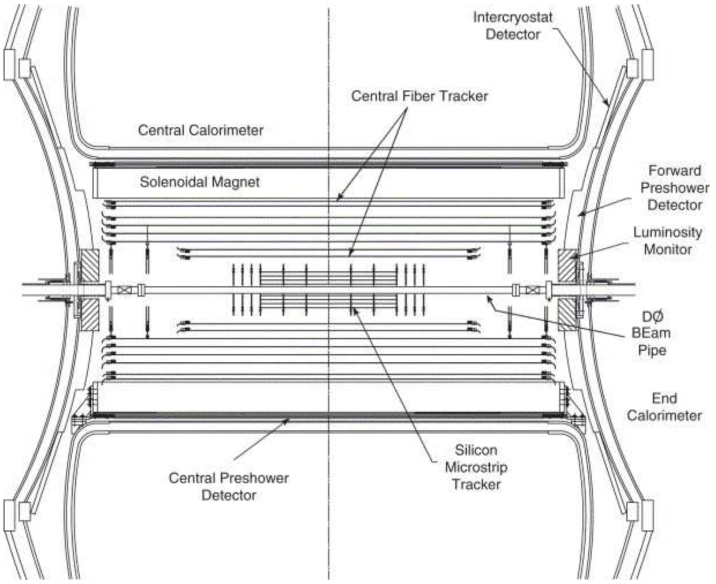

Figure 3–4: Sideview of the DØ tracking system [24].

of uranium, copper or stainless steel. Particles traversing the absorber plates subsequently enter the instrumented region which consists of electrodes submerged in liquid Argon. The charged particles ionise the liquid Argon which creates cascades of particles. Electrically charged particles are captured by the electrodes connected to high voltage. The recorded charge is proportional to the energy deposited in the active layer from traversing particles.

As shown in Figure 3–5, the DØ calorimeter consists of three sections: one central and two end parts. The central calorimeter has a cylindrical geometry that covers the pseudorapidity region $|\eta| < 1.1$. Both sides are flanked by end calorimeters which cover the pseudorapidity region $0.9 < |\eta| < 4.2$.

Each calorimeter section incorporates three module types: the electromagnetic layers, and the fine and coarse hadronic layers. Electromagnetic layers are closest to

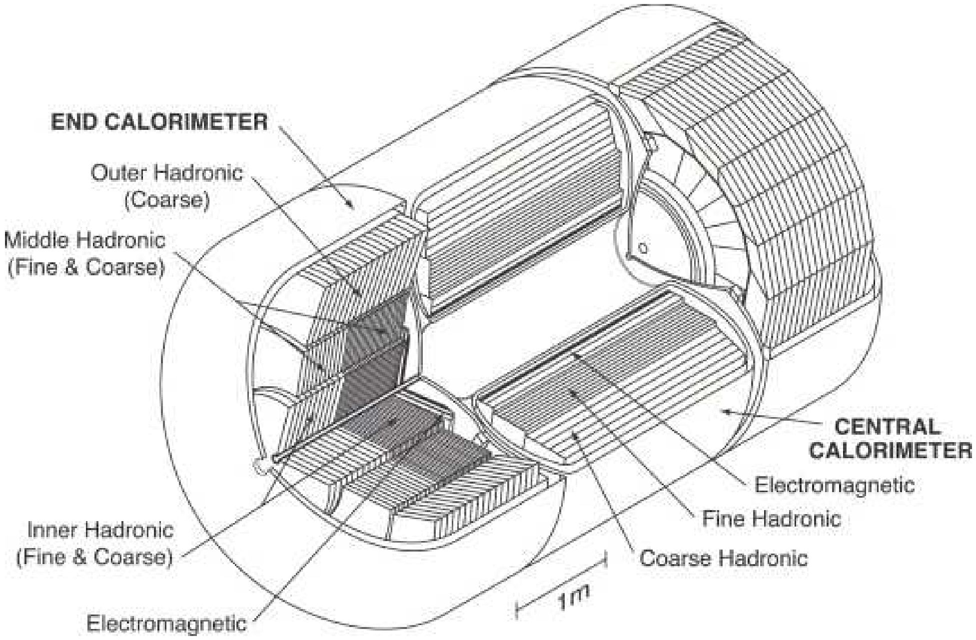

Figure 3–5: Schematic view of the DØ calorimeter [24].

the interaction point and use relatively thin absorber plates for the inactive material. Hadrons interact with the calorimeter mostly via nuclear processes [26] which result in fractional energy losses. Fractional energy losses for hadrons are smaller than the losses experienced by particles that mainly interact electromagnetically, e.g. electrons and photons. As a result, hadron showers develop over larger distances and tend to be more penetrating than showers induced by particles that mainly interact electromagnetically. The fine and course hadronic calorimeter layers are therefore composed of thicker absorber plates.

3.2.3 Muon Spectrometer

The muon spectrometer measures charged particle trajectories and provides an additional momentum measurement for muons that escape the detector. As shown in Figure 3–6, the spectrometer comprises two detector types: scintillation counters and muon drift tubes. The muon spectrometer is arranged in three layers around a toroidal magnet system, which makes it possible to measure the muon momentum. One layer is mounted on the inside of the magnet and the other two layers on the outside. The muon spectrometer measures muon trajectories in the pseudorapidity region $|\eta| < 2.0$. The magnet provides a 1.8 T toroidal field in the ϕ direction.

Scintillation Counters. Scintillation counters are made of square slabs of plastic that emit light when a charged particle traverses the material. The scintillation photons are captured by photmultiplier tubes for readout. Scintillation counters provide fast time response which is useful for the triggering process. In the central region, scintillation counters are located on both sides of the toroid magnet. The inside layer detects muons with low transverse momentum that are less likely to traverse the toroidal magnet. The outside layer is used together with the inside layer to trigger on muons associated with proton-antiproton collisions and to reject muons from cosmic rays [27]. Both layers of scintillation counters in the central region cover the pseudorapidity region $|\eta| \lesssim 1.0$. There are three layers of scintillation counters in the forward pseudorapidity region $1.0 \lesssim |\eta| \lesssim 2.0$. These counters are used to measure forward muon trajectories.

Muon Drift Chambers. Muon drift chambers [27] provide precise measurements of muon trajectories. The drift chambers are arranged in three layers and comprise proportional drift tubes in the central pseudorapidity region, $|\eta| \lesssim 1.0$, and mini-drift tubes in the forward region, $1.6 < |\eta| < 2.0$.

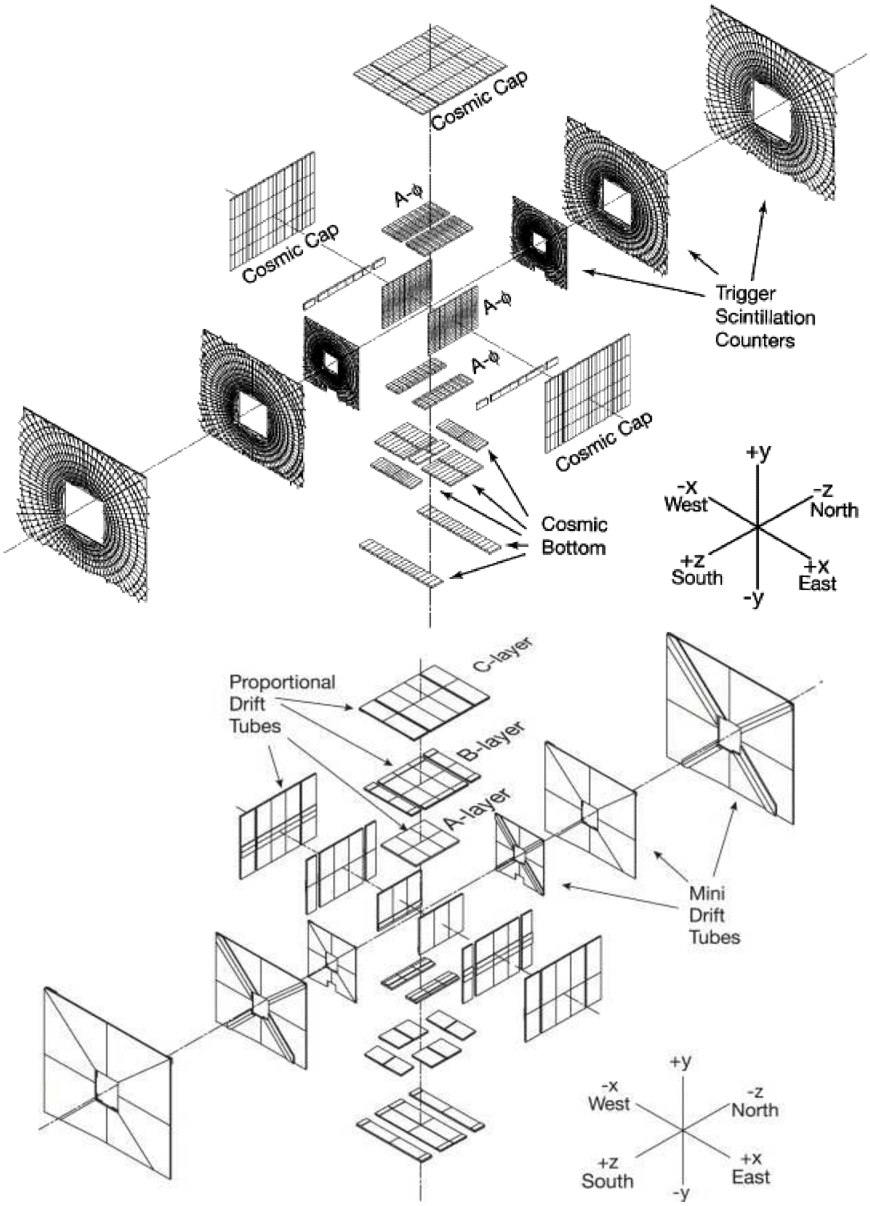

Figure 3–6: Schematic diagram of scintillation counters (top) and muon drift tubes (bottom) [24].

Drift chambers used in the muon system consist of gas-filled cavities with cathode pads on opposite sides. One anode wire is suspended in the centre of each cavity, parallel to the cathode pads. Cathode pads and anode wires are held at a high electric potential difference, creating an electric field. Charged particles traversing the cavity ionise the gas and form cascades of charged particles. Particles with negative electric charge migrate towards the anode wire, and particles with opposite charge migrate towards the cathode pads. The time difference between signal arrivals on both ends of anode wires, in addition to the integrated charge collected using the cathode pads are used for position measurements. The maximum electron drift time for a proportional drift tube cell is 450 ns, and the single wire coordinate resolution is approximately 1 mm. Corresponding numbers for a mini-drift tube cell are 132 ns and approximately 0.7 mm.

3.2.4 Trigger and Data Acquisition

The DØ trigger system works in real-time to filter events of potential interest for physics analysis. One effect of the filtering process is a decrease in the number of recorded events from the number of collisions delivered by the Tevatron. This filtering process helps avoid the saturation of limited storage space.

As shown in Figure 3–7, the trigger system works in three levels. The first trigger level (Level 1) uses hardware components that scan all incoming events for interesting features. Level 1 uses coarse information from different subdetector systems to reduce the nearly 2 MHz incoming rate by three orders of magnitude. The second trigger level (Level 2) uses programmable preprocessors, related to different detector subsystems, and makes initial reconstructions of physical observables.

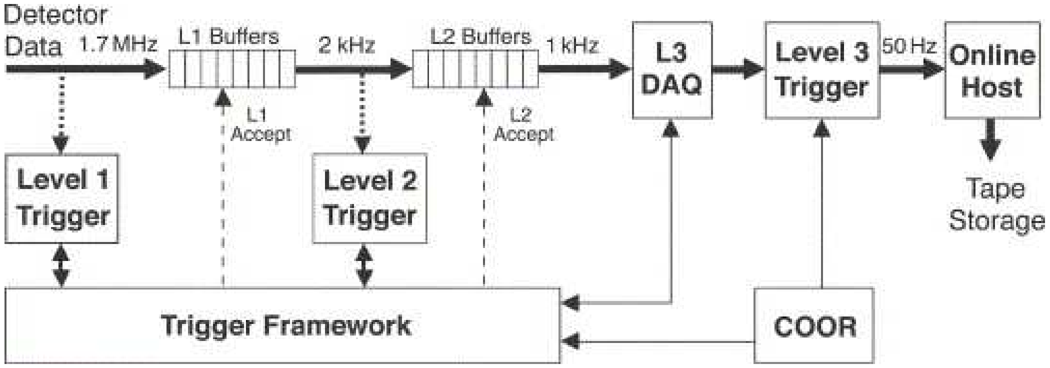

Figure 3–7: Overview of the trigger and data acquisition framework [24].

These observables are used by a Level 2 global processor which analyses correlations to construct global observables. This reduces the approximately 2 kHz input rate to an event acceptance rate near 1 kHz. Events that pass Level 2 are processed by a large computer farm of more than 200 nodes which comprises the third trigger level (Level 3). The computer farm uses complex software algorithms to reduce the input rate to 50-100 Hz. The Level 3 selected events are recorded to tape and used for offline analysis.

CHAPTER 4
Event Samples

This chapter gives a brief introduction to the data as well as simulated background and signal samples used in the analysis presented in this thesis. Further discussion on all samples is provided in Chapter 5.

DØ Data. Approximately 0.9 fb^{-1} of data recorded in proton-antiproton collisions at a centre-of-mass energy of $\sqrt{s} = 1.96$ TeV was used in the analysis presented in this thesis. The data set was recorded between August 2002 and December 2005.

Simulated Event Samples. Events in simulated samples were produced using Monte Carlo generators which incorporate appropriate physics theories to generate desired physics processes. After event production, a PYTHIA [28] based Monte Carlo generator was used to simulate hadronization processes for quarks and other unstable particles. The simulated event samples were then processed in a GEANT [29] based simulation program that models hadron shower processes and particle energy depositions in the DØ detector.

Simulated event samples used in this analysis represent the charged Higgs boson signal and most background sources. The simulated background samples used in this analysis include the production of W^+ bosons and associated jets (W+jets). Samples for the W+jets background source were produced with jets originating from light (Wjj) and heavy flavour quarks ($Wc\bar{c}$, $Wb\bar{b}$). Simulated background samples used in this analysis also include the production of top-antitop quark pairs ($t\bar{t}$). The

Table 4–1: Monte Carlo generators, total expected cross-sections and integrated luminosities for simulated samples used in this analysis [30]. Expected cross-sections are approximate. Cross-sections for Wjj, $Wc\bar{c}$, and $Wb\bar{b}$ background sources are not used in the analysis as will be explained in Section 5.4.

Simulated Samples	Monte Carlo Generator	Cross-Section (pb)	Integrated Luminosity (fb^{-1})
Wjj	ALPGEN [31]	$18,734$	1
$Wc\bar{c}$	ALPGEN	583	8
$Wb\bar{b}$	ALPGEN	142	28
$t\bar{t}$	ALPGEN	6.8 ± 1.2	249
tb, tqb	SingleTop [32]	2.86 ± 0.45	709

remaining simulated background samples used in this thesis are the production of top and bottom quarks through W^+ boson decays (commonly referred to as single top events). The single top events were simulated in the s-channel (tb) and t-channel (tqb). Table 4–1 summarises the simulated background event samples used in this analysis, Monte Carlo generators used to generate the samples, total cross-sections and integrated luminosities.

Charged Higgs Signal Samples. The s-channel charged Higgs boson production process in the signal samples is illustrated in the Feynman diagram in Figure 4–1. Charged Higgs boson signal samples were produced using the CompHEP Monte Carlo generator [11]. Subsequently, charged Higgs bosons were forced to decay to top and bottom quarks. Top quarks decay to a W^+ boson and a bottom antiquark with a greater than 99% probability [1]. During signal generation, W^+ bosons from top quark decays were forced to decay leptonically: $W^+ \rightarrow e^+\nu_e, \mu^+\nu_\mu, \tau^+\nu_\tau$. Signal samples were produced for seven charged Higgs boson masses (M_{H^+} = 180, 200, 220,

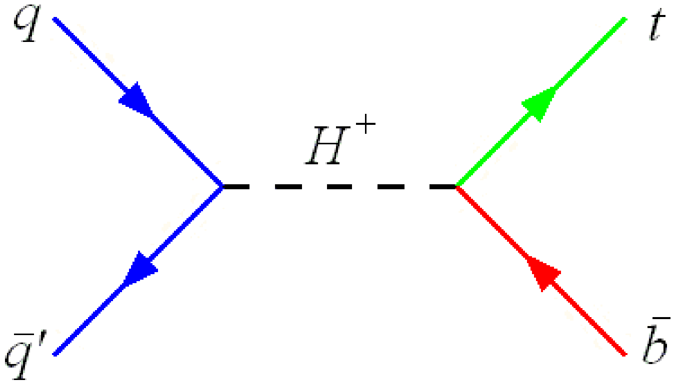

Figure 4–1: Leading order Feynman diagram for quark fusion production of a charged Higgs boson with decay to top and bottom quarks.

240, 260, 280, 300 GeV/c^2). The lower 180 GeV/c^2 mass bound is near the minimum mass requirement that allows charged Higgs bosons to decay to top and bottom quarks. The upper 300 GeV/c^2 mass bound is motivated by the expected decline of the charged Higgs boson production cross-section as the mass of the charged Higgs boson increases. Figure 2–1 shows examples of decreasing cross-sections for parameters $\tan\beta = 100$, $\tan\beta = 0.1$ and $\xi = 5$ in Types I, II and III 2HDMs, respectively. In these different scenarios, the charged Higgs boson production cross-section decreases significantly as the mass of the charged Higgs boson increases from 180 GeV/c^2 to 300 GeV/c^2.

The effective 2HDM Lagrangian given by Equation 2.3 was used to generate the signal samples. Samples with pure left-handed (L) or pure right-handed (R) chiral state processes were produced by setting the couplings to ($c_L^{ij} = V_{\text{CKM}}^{ij} g_w, c_R^{ij} = 0$) or ($c_L^{ij} = 0, c_R^{ij} = V_{\text{CKM}}^{ij} g_w$), respectively. Left-handed and right-handed samples were combined in different proportions to simulate a particular 2HDM type. Event weights

($w_{\mathrm{L/R}}$) were calculated as

$$w_{\mathrm{L/R}} = \frac{\sigma_{\mathrm{L/R}}}{\sigma} \tag{4.1}$$

where $\sigma_{\mathrm{L/R}}$ is the charged Higgs boson production cross-section assuming pure left-handed/right-handed chiral states and σ represents the total model dependent charged Higgs boson production cross-section. The event weights are shown in Table 4–2.

In the charged Higgs boson production cross-section for Types I and II 2HDMs, the interference between left-handed (c_L^{ij}) and right-handed (c_R^{ij}) couplings is proportional to $c_L^{ij} c_R^{ij} m_i m_j / m_{H^+}^2$ [10]. The size of the interference term is suppressed by the charged Higgs boson mass if the product of the couplings c_L^{ij} and c_R^{ij} is small. For the Type I 2HDM and for all $\tan\beta$ values, the size of the interference term is negligible relative to the sizes of both the couplings c_L^{ij} and c_R^{ij}. For the Type II 2HDM and for all $\tan\beta$ values, the size of the interference term is negligible relative to the size of the coupling c_R^{ij}. The size of the interference term is negligible relative to the size of c_L^{ij} for values $\tan\beta \lesssim 30$. For larger $\tan\beta$ values, the interference term becomes greater than c_L^{ij}. Since the event weight of the left-handed signal sample is very small, the interference term can be ignored also for the Type II 2HDM for all $\tan\beta$ values. For the Type III 2HDM, the couplings are almost purely right-handed and the interference term is negligible. The interference between left-handed and right-handed couplings is small for Types I, II and III 2HDMs, for all parameter values considered in this analysis, hence the fact that the weighting approach used

Table 4–2: Event weights of left-handed (L) and right-handed (R) signal samples that were used to simulate Types I, II and III 2HDMs. These weights were calculated for $\tan\beta < 0.1$, $\tan\beta = 1$, $\tan\beta = 5$ and $\tan\beta > 10$, and are applicable for all charged Higgs boson masses in the analysis. The Type III 2HDM does not depend on the $\tan\beta$ parameter.

		$\tan\beta < 0.1$	$\tan\beta = 1$	$\tan\beta = 5$	$\tan\beta > 10$
2HDM (I)	L	0.5	0.5	0.5	0.5
	R	0.5	0.5	0.5	0.5
2HDM (II)	L	0.99999	0.5	0.002	0.00001
	R	0.00001	0.5	0.998	0.99999

2HDM (III)	L	0
	R	1.0

in this analysis did not take interference into account did not significantly affect the final results.

CHAPTER 5
Event Selection

This analysis consists of a search for charged Higgs bosons decaying to top and bottom quarks. Furthermore, the search focuses on leptonic final states, as shown in the Feynman diagram in Figure 5–1. In this chapter, necessary steps to identify events with the charged Higgs boson signal signature are described: the reconstruction of physical observables in Section 5.1 and kinematic event selection requirements in Section 5.2. Data samples are briefly described in Section 5.3. The background modelling and the identification of jets originating from *b* quarks are described in Sections 5.4 and 5.5, respectively. Finally, the charged Higgs boson signal selection efficiency is quantified in Section 5.6.

Several scaling factors for Monte Carlo simulated events were implemented to correct for differences between real and simulated DØ detector efficiencies. Reference [33] provides a detailed description of these.

5.1 Object Reconstruction

Standard DØ definitions were used to reconstruct observables in each of the data, background and charged Higgs boson signal events. Reconstructed objects used in this analysis are the primary vertex, electrons, muons, jets and missing transverse energy.

Primary Vertex. The primary vertex is the reconstructed location of the hard scattering interaction in proton-antiproton collisions. An iterative primary vertex reconstruction algorithm [34] was used. The initial step consisted of clustering reconstructed particle trajectories to common vertex locations. All reconstructed particle trajectories were then subject to an iterative fitting process that assigned weights to trajectories according to their distance from their vertex position.[1] Each reconstructed particle trajectory was initially assigned the weight 1.0. The fitting procedure continued until the weights converged to a value that did not significantly change after each iteration. Finally, the weights were used to determine the probability that each vertex represented a minimum bias interaction.[2] The vertex with the smallest probability value was chosen as the primary vertex.

Electrons. Electrons were identified using an algorithm [35] that checked for consistencies between the expected shape of electromagnetic showers from electrons and clusters of energy deposited in the electromagnetic layers of the central calorimeter [33]. Electrons also require the identification of a charged particle trajectory detected in the central tracking system, associated with the centre of the calorimeter cluster. Two kinds of quality definitions were used. Electrons of a loose quality

---

[1] In this method, all reconstructed particle trajectories contribute to the primary vertex with different weights ranging from 0 to 1. The larger the weight, the smaller is the distance of closest approach between the particle trajectory and the primary vertex.

[2] A minimum bias interaction is used here to refer to any inelastic collisions in the Tevatron.

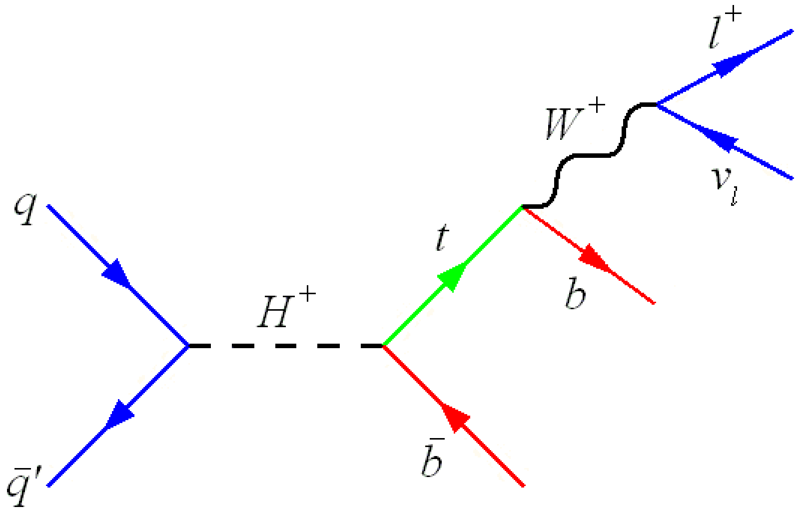

Figure 5–1: Feynman diagram of the charged Higgs boson signal signature: one charged lepton, one neutrino and two bottom quarks.

had at least 90% of their total energy deposited in the electromagnetic layers of the calorimeter. Electrons of a tight quality constituted a subset of loose electrons, and, in addition, had to satisfy a minimum value of a likelihood function [36]. The likelihood function defines a probability that an object is an electron based on information from the calorimeter and the central tracking system.

Muons. The muon identification algorithm [37] reconstructed muons using hits detected in all three layers of the muon spectrometer. These hits were required to be associated with a charged particle trajectory in the central tracking system and with no significant amount of energy deposited in the calorimeter. Two kinds of isolation definitions were implemented. Muons with loose isolation had to satisfy a minimum ΔR distance requirement[3] away from nearby jets. The ΔR distance requirement was implemented in order to be consistent with charged Higgs boson decays to top and bottom quarks where the muon from the W boson decay and the jets that originate from b quarks are expected to be distinctly separated. Muons with loose isolation also had to satisfy a timing requirement that ruled out cosmic background muons. Tight muons were loose muons that satisfied additional requirements in the way in which energy and momentum were distributed near the muon trajectory. Muons were not expected to decay and leave additional tracks along its trajectory in the DØ detector. The energy deposited in calorimeter cells and the combined momentum of trajectories near the trajectory associated with the track matched with the muon must be small with respect to the reconstructed energy and momentum, respectively, of the muon.

Jets. The jet reconstruction algorithm [38] identified cone shaped regions in the calorimeter where a significant amount of energy was deposited as jets. Jets containing three-dimensionally isolated regions of deposited energy in the calorimeter were not consistent with the expected cone-like shape of a jet and were therefore rejected by the jet removal algorithm [39].

Missing Transverse Energy. Neutrinos escape the DØ detector without leaving a signal. Rather than using direct detection, the presence of neutrinos was

---

[3] The distance between two objects in (ϕ, η) space is defined as $\Delta R = \sqrt{(\Delta\phi)^2 + (\Delta\eta)^2}$.

inferred through their undetected energy contribution in an event. Assuming momentum conservation in the transverse plane, the transverse neutrino momentum component was defined as the negative of the vectorial sum of the transverse momenta of all detected particles. The magnitude of the vector sum was equivalent to the missing transverse energy carried by the neutrino since its mass was assumed to be negligible.

5.2 Preselection

The expected final state particles in charged Higgs boson production and single top s-channel processes are precisely the same. Kinematic event selection requirements, called preselection cuts, for the DØ single top quark search [40] were therefore re-used in this analysis. Preselection cuts were applied at the event level and on individual reconstructed objects in data and Monte Carlo simulated events. These cuts were developed to select events with one isolated lepton, missing transverse energy and two jets with high transverse momentum. The event preselection is characterised by loose selection criteria aimed to maximise the single top signal acceptance. Due to the similarities between charged Higgs boson and single top signal signatures, the preselection cuts maximise the signal acceptance also for charged Higgs boson candidate events. More details about the preselection cuts are presented in Appendix A.

Preselection cuts also select events where W^+ bosons decay to a tau and a neutrino, and where the tau further decays to an electron or muon. These events in the tau decay mode contributed to 3-8% of the total preselected charged Higgs boson signal events.

5.3 Data Samples

Given the similarities between final state particles, data samples analysed in the DØ single top search were re-used in this analysis. The data were selected using trigger criteria [41] that required one lepton and a jet in each event where the lepton was either an electron or muon.[4] For electron events, the trigger selection required one single electromagnetic energy cluster and a jet in the calorimeter. For muon events, the trigger selection required one single muon and a jet. The integrated luminosity of data analysed for the electron and muon data samples amounted to 913 pb^{-1} and 871 pb^{-1}, respectively.

5.4 Background Modelling

The methods used in this analysis to estimate background contributions were identical to methods that were used in the DØ single top analysis [33]. The background sources in this analysis were in order of importance W+jets, multijet, $t\bar{t}$ and single top events. The W+jets background events contained W^+ bosons and associated jets originating from light quarks (u, d, s) or heavy quarks (c, b). The final state in the W+jets events include leptons from the W^+ boson decay and associated jets. These objects are identical to the objects in the charged Higgs boson signal signature which is why the W+jets events form a background. The shapes of the W+jets background distributions were obtained from Monte Carlo simulated event

---

[4] Events where the lepton was identified as an electron or a muon will in the remainder of this thesis be referred to as electron or muon channel events, respectively.

samples listed in Table 4–1. The expected number of W+jets background events was normalised to data using a normalisation method described below.

A large multiplicity of quantum chromodynamic processes are responsible for the multijet background in this analysis. In these events, one of the jets was misidentified as a lepton[5] and the misreconstruction of objects resulted in false missing transverse energy. Containing one false lepton, missing transverse energy and jets, multijet events mimicked the charged Higgs boson signal signature and formed a source of background events. The use of Monte Carlo techniques to accurately simulate the multijet background is a practical challenge that was not attempted in this analysis. The shapes of the multijet background distributions were obtained from an orthogonal fake-lepton data sample, where one of the jets satisfied a loose, but not tight, lepton isolation quality.[6] The orthogonal data sample was normalised to the number of fake-lepton events contained in preselected data. This amount was obtained using a normalisation technique, called the matrix method, which is described in [33, 42]. Events containing real leptons with loose isolation quality were mainly W+jets and $t\bar{t}$ events [33]. The number of these events was multiplied by the probability that a real lepton passed the tight isolation quality requirements. This product was incorporated in the matrix method to estimate the number of W+jets and $t\bar{t}$ events

---

[5] The lepton was an electron or a muon in the electron or muon channels, respectively.

[6] A study has shown that the orthogonal fake-lepton sample contained an insignificant amount of events with properly identified leptons [33].

containing tight leptons. The number of W+jets events containing tight leptons was obtained by subtracting the estimated number of $t\bar{t}$ events containing tight leptons (explained below) from the estimated total number of W+jets and $t\bar{t}$ events containing tight leptons. The number of W+jets events containing tight leptons was used as the normalisation factor for the simulated W+jets samples.

The $t\bar{t}$ sample contained events with pair-produced top-antitop quarks. Monte Carlo samples were generated for two decay modes; one where the W^+ boson from the decay of the top quark decayed leptonically (or hadronically), and the W^- boson from the decay of the antitop quark decayed hadronically (or leptonically). Leaving one lepton, one neutrino and jets in the final states, this decay mode formed a background since it contained the same final state particles as in the charged Higgs boson signal. The other decay mode represented events where both W^+ and W^- bosons underwent leptonic decays, leaving two charged leptons, two neutrinos and two jets in the final state. This $t\bar{t}$ sample formed a background, in cases where only one of the charged leptons were identified. The shape of the $t\bar{t}$ background sources were obtained from $t\bar{t}$ Monte Carlo samples. Both samples were normalised to next-to-leading order cross-sections from theoretical calculations.

The single top events were the smallest background contribution which represented the production of top and bottom quarks through W^+ boson decays. Single top samples were simulated for the s-channel (tb) and t-channel (tqb) processes. The simulated single top samples provided the shape of the background distributions and were normalised to the expected theoretical cross-sections.

The background modelling resulted in good agreement with data samples in both electron and muon channels. Figure 5–2 shows examples of data-background comparisons of different kinematic variables.

5.5 *b* Tagging

The b tagging algorithm [33, 43] identified jets originating from b quarks (b jets). This algorithm was applied to maximise the ratio of the number of charged Higgs boson events over the total number of background events. The b tagging algorithm looked for jets with an associated secondary vertex which represents the decay of a B meson. A brief description of the differences between b tagging methods for data and simulated events is provided in Appendix B.

The final analysis presented in this thesis included events with one or two jets identified as b jets. This requirement resulted in a significant decrease in the dominant W+jets background, the Wjj contribution, from 69% to 15% of the total background. Background sources containing b jets in the final state became more important after b tagging. For instance, the $Wb\bar{b}$ contribution increased from 4.6% to 36% of the total background.

The signal significance is defined as the ratio of the charged Higgs boson signal yield to the total yield of all background sources. After b tagging, the total signal significance increased by a factor of approximately 12 for all mass cases.

Background and data samples remained in good agreement after b tagging. Figure 5–3 shows examples of data-background sample comparisons of the same kinematic variables shown in Figure 5–2 after b tagging. The events in data, background

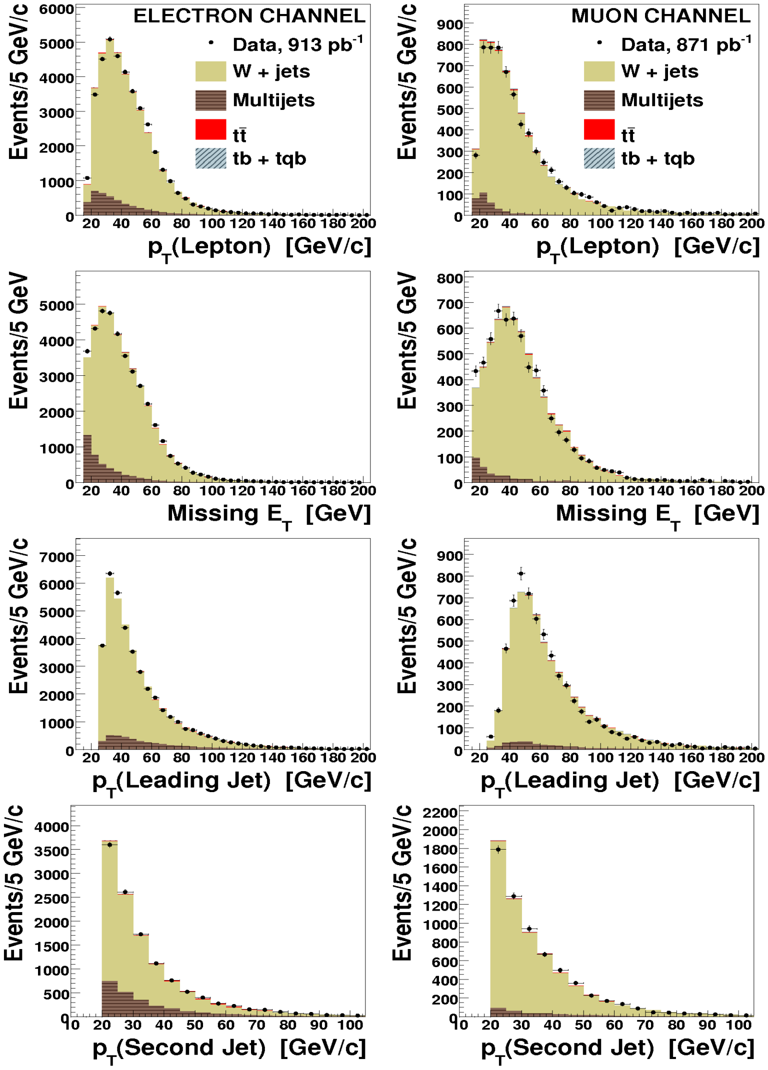

Figure 5–2: Comparison plots for data and background samples after preselection cuts. Kinematic variables shown here for the electron (left column) and muon channels (right column) are: the transverse momentum of the lepton, missing transverse energy in the event, and transverse momentum of the most energetic jet (leading jet) and the second most energetic jet (second jet). After preselection cuts, the combined expected contribution from $t\bar{t}$ and single-top background sources relative to the sum of the total background is at the percent level. The $t\bar{t}$ and single-top background contributions are too small to be clearly visible in these histograms.

and charged Higgs boson signal samples were divided into four different and independent analysis channels which are: electron or muon events with either one or two b tagged jets.

5.6 Event Yield and Signal Acceptance

The data event yield is the number of events that pass each selection requirement. Table 5–1 shows event yields after preselection, one and two b tag requirements. These values show that b tagging requirements significantly reduced the dominant background sources and that the largest background became the $Wb\bar{b}$ contribution.

The charged Higgs signal acceptance, $\mathcal{A}_{\text{signal}}$, is calculated in the DØ single top group as

$$\mathcal{A}_{\text{signal}} = \frac{\mathcal{B}}{N_{\text{initial}}} \sum_{N_{\text{presel}}} \epsilon_{\text{trigger}} \epsilon_{\text{correction}} \epsilon_{b-\text{tagging}} \tag{5.1}$$

where $\mathcal{B}$ is the branching ratio of the leptonic W^+ boson decay, N_{initial} is the initial number of events in the Monte Carlo sample, and N_{presel} represents the events that pass the event selection. The symbol $\epsilon_{\text{trigger}}$ represents the trigger efficiency for each event, $\epsilon_{\text{correction}}$ is the product of correction factors which incorporate differences between Monte Carlo and data events, and $\epsilon_{b-\text{tagging}}$ is the probability for each event to have one b tagged jet or more [44]. The product of these efficiencies form an event weight which is summed for the N_{presel} events that pass the preselection. Table 5–2 presents signal acceptances for Types I, II and III 2HDMs.

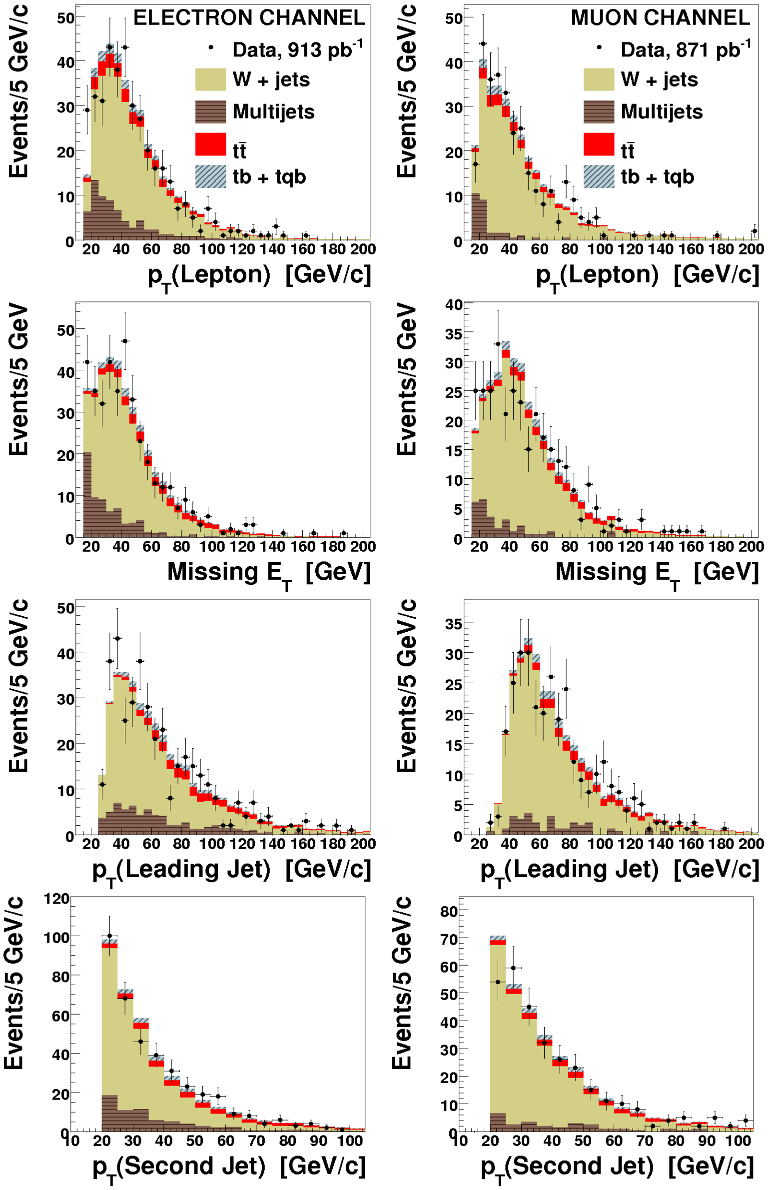

Figure 5–3: Comparison plots for data and background samples after b tagging. Kinematic variables shown here for the electron (left column) and muon channels (right column) are: the transverse momentum of the lepton, missing transverse energy in the event and transverse momentum of the most energetic jet (leading jet) and the second most energetic jet (second jet).

Table 5–1: Number of events in the electron and muon channels after the preselection and b tagging requirements. Values in the last two columns represent the number of events in samples that fulfil the requirement where exactly one or exactly two jets per event originated from b quarks. These values were taken from [33].

Event Type	Preselection	1 b-tag	2 b-tags
BACKGROUND			
$Wjj \to l\nu jj$	10160	119	0.2
$Wc\bar{c} \to l\nu cc$	1959	148	3.2
$Wb\bar{b} \to l\nu bb$	670	230	31.5
Multijets	1762	92	4.0
$t\bar{t} \to l$+jets	40	17	2.7
$t\bar{t} \to ll$	62	29	10.1
$tb, tqb \to l$+jets	72	32	4.7
Background Sum	14725	667	56
DATA	14652	644	53

5.7 Systematic Uncertainties

Systematic uncertainties were divided into two kinds: uncertainties only affecting the overall number of events and uncertainties affecting both the kinematic properties and number of events. Systematic and statistical uncertainties considered in this analysis and their estimated values are summarised in Appendix C. A detailed description of the methods of estimation for all systematic uncertainties is provided in [33].

The largest systematic uncertainties for background events were the uncertainties on jet energy scale, tag-rate functions,[7] cross-section estimations and normalisation of W+jets and multijet backgrounds. Uncertainties on the jet energy scale and

---

[7] Tag-rate functions were used to identify jets that originated from b quarks in Monte Carlo simulated events, as briefly described in Appendix B.

Table 5–2: Acceptances in percent for Type II 2HDM signal events. These acceptances were calculated for all combined analysis channels. Acceptances obtained for $\tan\beta = 1$ and $\tan\beta > 10$ apply also for Types I and III 2HDMs, respectively. Acceptances are presented with the statistical (first) and systematic (second) uncertainties described in Section 5.7.

$M_{H^\pm}$ (GeV/c^2)	$\tan\beta < 0.1$	$\tan\beta = 1$
180	$(0.48 \pm 0.01 \pm 0.08)\%$	$(0.47 \pm 0.01 \pm 0.08)\%$
200	$(0.41 \pm 0.01 \pm 0.07)\%$	$(0.41 \pm 0.01 \pm 0.07)\%$
220	$(0.73 \pm 0.02 \pm 0.12)\%$	$(0.70 \pm 0.02 \pm 0.11)\%$
240	$(1.00 \pm 0.02 \pm 0.16)\%$	$(0.94 \pm 0.02 \pm 0.15)\%$
260	$(1.11 \pm 0.02 \pm 0.18)\%$	$(1.01 \pm 0.02 \pm 0.17)\%$
280	$(1.18 \pm 0.02 \pm 0.19)\%$	$(1.11 \pm 0.02 \pm 0.18)\%$
300	$(1.24 \pm 0.02 \pm 0.20)\%$	$(1.18 \pm 0.02 \pm 0.19)\%$
$M_{H^\pm}$ (GeV/c^2)	$\tan\beta = 5$	$\tan\beta > 10$
180	$(0.46 \pm 0.01 \pm 0.07)\%$	$(0.46 \pm 0.01 \pm 0.07)\%$
200	$(0.40 \pm 0.01 \pm 0.06)\%$	$(0.40 \pm 0.01 \pm 0.06)\%$
220	$(0.68 \pm 0.02 \pm 0.11)\%$	$(0.68 \pm 0.02 \pm 0.11)\%$
240	$(0.89 \pm 0.02 \pm 0.14)\%$	$(0.89 \pm 0.02 \pm 0.14)\%$
260	$(1.00 \pm 0.02 \pm 0.16)\%$	$(1.00 \pm 0.02 \pm 0.16)\%$
280	$(1.01 \pm 0.02 \pm 0.17)\%$	$(1.01 \pm 0.02 \pm 0.17)\%$
300	$(1.12 \pm 0.02 \pm 0.18)\%$	$(1.12 \pm 0.02 \pm 0.18)\%$

tag-rate functions were the only ones affecting both the shape and normalisation of kinematic distributions.

For the charged Higgs boson signal, all uncertainties were assumed to be the same as in the single top signal with the exception of the uncertainties on the jet energy scale and on the tag-rate functions that were re-calculated using the method described in [33]. The largest systematic uncertainties for the charged Higgs boson signal were the uncertainties on the cross-section, jet energy scale, tag-rate functions and the initial state parton contribution (described below).

The coupling between the charged Higgs boson and the initial state partons is specific to the 2HDM type, as described by Equations 2.4−2.9. Since samples were not produced using model specific couplings (see discussion in Section 4), the sensitivity to changes in initial state parton flavour combinations was assessed. Charged Higgs boson signal samples were studied where the initial state parton flavour pair was fixed to either $u\bar{d}, u\bar{s}, u\bar{b}, c\bar{d}, c\bar{s}$ or $c\bar{b}$. These exclusive samples were subject to the analysis selection chain and their event yields were studied. The standard deviation divided by the mean of the event yield (σ/μ) for each exclusive initial state parton flavour combination was calculated. For the two chirality states and both lepton channels, σ/μ varied between 4.3% and 6.8%. On the basis of these values, and on two types of additional cross-checks explained in [10], a flat 10% systematic uncertainty was used for the unknown proportion of initial state parton flavour pairs. In one of the two cross-checks, the percent difference between each exclusive sample and the $c\bar{b}$ exclusive sample in each bin of the reconstructed invariant mass distribution was calculated.

CHAPTER 6
Analysis and Results

No excess of data over background was observed and upper limits on the charged Higgs boson production cross-section were derived. The upper limits were translated into exclusion regions in $(M_{H^+}, \tan\beta)$ parameter space. In Section 6.1, the discriminating variable used for setting charged Higgs production cross-section times branching fraction limits is described. The experimental resolution on the discriminating variable is described in Section 6.2. Upper limits on the cross-section times branching ratio for Types I, II and III 2HDMs are provided in Section 6.3 and parameter constraints for the Type I 2HDM are described in Section 6.4.

6.1 The Discriminating Variable

The expected large mass of the charged Higgs boson studied in this analysis provided a distinctive feature in the signal events. Furthermore, the reconstructed invariant mass was shown to be the most sensitive variable in that it was the variable that lead to the lowest expected upper limits on the charged Higgs boson production cross-section. For these reasons, the reconstructed invariant mass was used as the discriminating variable to separate the charged Higgs boson signal from the background in this analysis. The reconstructed invariant mass of the top and bottom quark system was obtained by adding the 4-vectors of the two jets and the reconstructed W^+ boson for each event. The W^+ boson was reconstructed by adding the 4-vectors of the lepton and the missing transverse energy. Figure 6–1 shows the

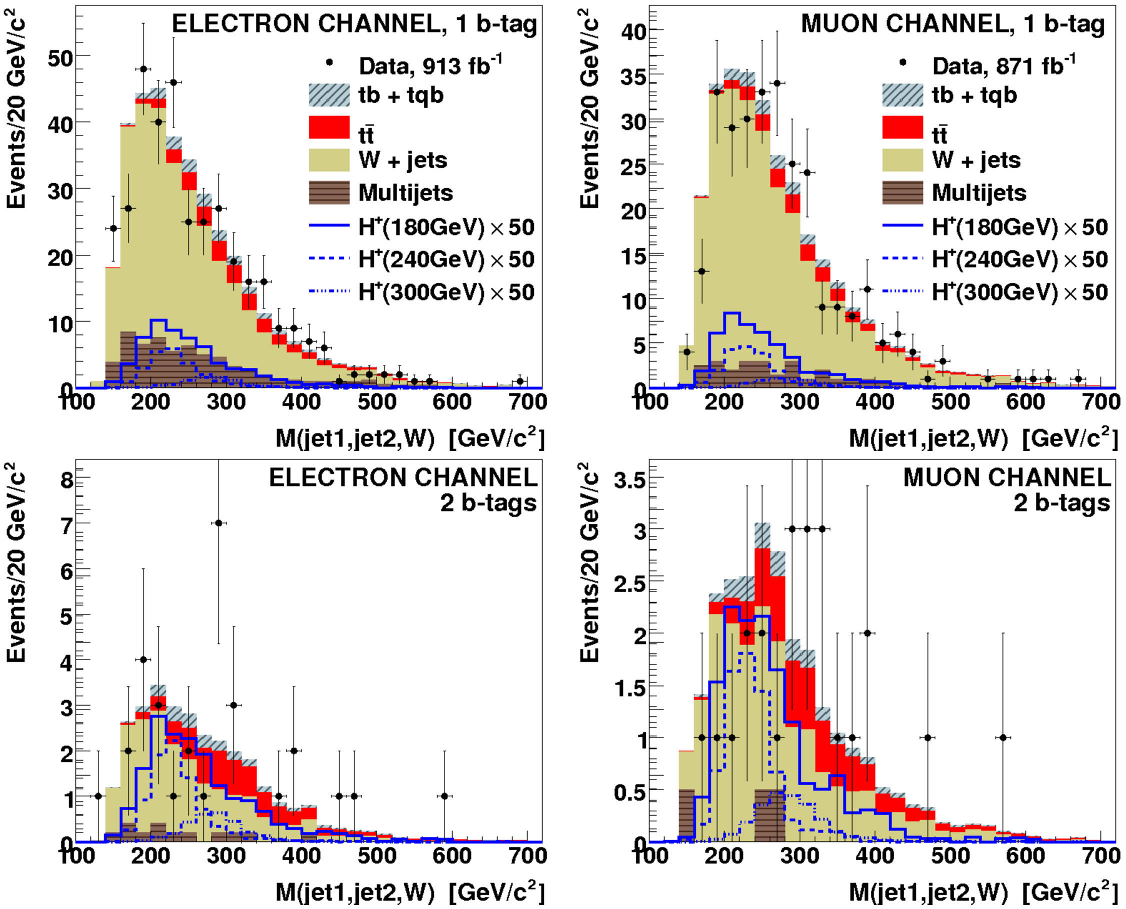

Figure 6–1: Reconstructed invariant mass distributions for electron (left column) and muon (right column) analysis channels, containing exactly one or two jets originating from b quarks. The signal distributions correspond to the Type III 2HDM for charged Higgs boson masses $M_{H^+} = 180$, 240, 300 GeV/c^2. These distributions were normalised according to the production cross-section presented in [9] and scaled by a factor of 50.

reconstructed invariant mass distributions for data, background and charged Higgs boson events.

6.2 Experimental Resolution

The shape of the reconstructed invariant mass distribution of the charged Higgs boson is sensitive to its total width if the total width is greater than the experimental resolution. Both the total width and detector resolution can therefore affect the overall shape of the reconstructed invariant mass distribution. In this analysis, the approach used to simulate the production of a charged Higgs boson signal did not take into account the dependence on the total width of the charged Higgs boson. This analysis is therefore valid only for points in parameter space where the total charged Higgs boson width is smaller than the experimental resolution.

A Gaussian fit of the reconstructed invariant mass distribution gave a root mean square of 25 GeV/c^2 for the 200 GeV/c^2 charged Higgs boson in the Type II 2HDM with $\tan\beta = 1$ [10]. The CompHEP simulated total width of a charged Higgs boson with the same parameter values was approximately 5 GeV. These values resulted in a reconstructed experimental resolution for the invariant mass variable approximately equal to $\sqrt{25^2 - 5^2}$ GeV/c^2 $\approx$ 25 GeV/c^2.[1] This value was assumed as the experimental resolution for Types I, II and III 2HDMs. This analysis was valid for different 2HDM types and for $\tan\beta$ parameter values where total widths were significantly smaller than the experimental resolution. As a result, the analysis was valid for the Type I 2HDM in the 200 GeV/c^2 mass case for $\tan\beta < 10$. The total width for the Type II 2HDM increased beyond the experimental resolution for charged Higgs boson masses $M_{H^+} \gtrsim 200$ GeV/c^2 in the parameter region $\tan\beta < 0.1$. The total width for the Type III 2HDM was significantly smaller than the experimental resolution in the parameter region $\xi < 1.0$.

6.3 Cross-Section × Branching Ratio Limits

Reconstructed invariant mass distributions for data, background and charged Higgs boson signal samples were analysed using a Bayesian statistical approach. The statistical approach was implemented using a standard DØ software package [45] to derive upper limits on the charged Higgs boson production cross-section times branching ratio to the top and bottom quark final state. This statistical approach

---

[1] Near peak values, the invariant mass distribution for the data sample and the experimental resolution were assumed to follow Gaussian distributions and the former was extracted using a Gaussian fit approximation. The data distribution was defined as the convolution of the functions for the experimental resolution and the width of the charged Higgs boson decay to top and bottom quarks. The charged Higgs boson width was assumed to follow a Gaussian distribution hence it followed that the square of the standard deviation of the data (σ_{data}) was defined as the sum of the square of the width of the experimental resolution (σ_{expt}) and the square of the expected width of the charged Higgs boson ($\sigma_{H^+\text{width}}$). The experimental resolution was calculated according to the equation $\sigma_{\text{expt}} = \sqrt{\sigma^2_{\text{data}} - \sigma^2_{H^+\text{width}}}$.

exploited the discrimination power contained in the reconstructed invariant mass distributions which would be ignored if basing the limits on total sample event counts only. An overview of the statistical approach is included in Appendix D.

Upper limits were derived at the 95% confidence level for all analysis channels combined for Types I, II and III 2HDMs in the mass range $180 \leq M_{H^+} \leq 300$ GeV/c^2. Table 6–1 shows observed and expected upper limits obtained including systematic uncertainties. Small kinematic differences between left-handed and right-handed chiral states resulted in a weak sensitivity of the cross-section times branching fraction limits to differences between 2HDM types [10]. A stronger limit sensitivity was seen depending on the charged Higgs boson mass case. The sensitivity increased for larger mass cases since the invariant mass distributions shifted towards larger mass values when the reconstructed mass of the charged Higgs boson increased. This shift resulted in a better separation from the total background distribution. Figure 6–2 shows plots for observed and expected upper limits for different 2HDMs as function of charged Higgs boson mass.

6.4 Model Parameter Constraints

Observed upper limits on the charged Higgs boson production cross-section were compared to expected signal cross-sections. This comparison resulted in excluded regions in $(M_{H^+}, \tan\beta)$ parameter space for the Type I 2HDM. Figure 6–3 shows the 95% confidence level exclusion region obtained for the Type I 2HDM.

Valid upper limits for Type II 2HDM cross-sections (see Table 6–1) did not exclude the production of charged Higgs bosons in $(M_{H^+}, \tan\beta)$ parameter space below $\tan\beta = 100$. This analysis was invalid for the Type II 2HDM in parameter regions

Table 6–1: Observed upper limits on the charged Higgs boson production cross-section (in pb) times branching ratio $\sigma(q\bar{q}' \to H^+) \times \mathcal{B}(H^+ \to t\bar{b})$ at the 95% confidence level. The expected limits are shown in parenthesis for comparison. The values represent combined limits for all analysis channels and apply to the Type II 2HDM. Limits obtained for $\tan\beta = 1$ and $\tan\beta > 10$ also apply for the Type I and III 2HDMs, respectively. Invalid upper limits due to the charged Higgs total width being larger than the experimental resolution are shown in square brackets. These limits can be useful for the general production of a charged scalar with a total width smaller than the experimental resolution.

$M_{H^\pm}$ (GeV/c^2)	$\tan\beta < 0.1$	$\tan\beta = 1$	$\tan\beta = 5$	$\tan\beta > 10$
180	12.9 (11.4)	14.3 (12.2)	13.7 (11.7)	13.7 (11.7)
200	[5.9 (9.6)]	6.3 (9.9)	6.5 (10.0)	6.5 (10.0)
220	[2.9 (4.2)]	3.0 (4.4)	3.0 (4.5)	3.0 (4.5)
240	[2.3 (3.1)]	2.4 (3.3)	2.6 (3.5)	2.6 (3.5)
260	[3.0 (2.8)]	3.0 (2.9)	3.0 (3.0)	3.0 (3.0)
280	[4.0 (2.6)]	4.2 (2.7)	4.5 (2.9)	4.5 (2.9)
300	[4.5 (2.4)]	4.7 (2.4)	4.9 (2.5)	4.9 (2.5)

$\tan\beta > 100$ where the charged Higgs boson width is larger than the experimental resolution. For the Type III 2HDM, this analysis did not exclude the production of charged Higgs bosons for values in (M_{H^+}, ξ) parameter space where the expected width was significantly smaller than the experimental resolution.

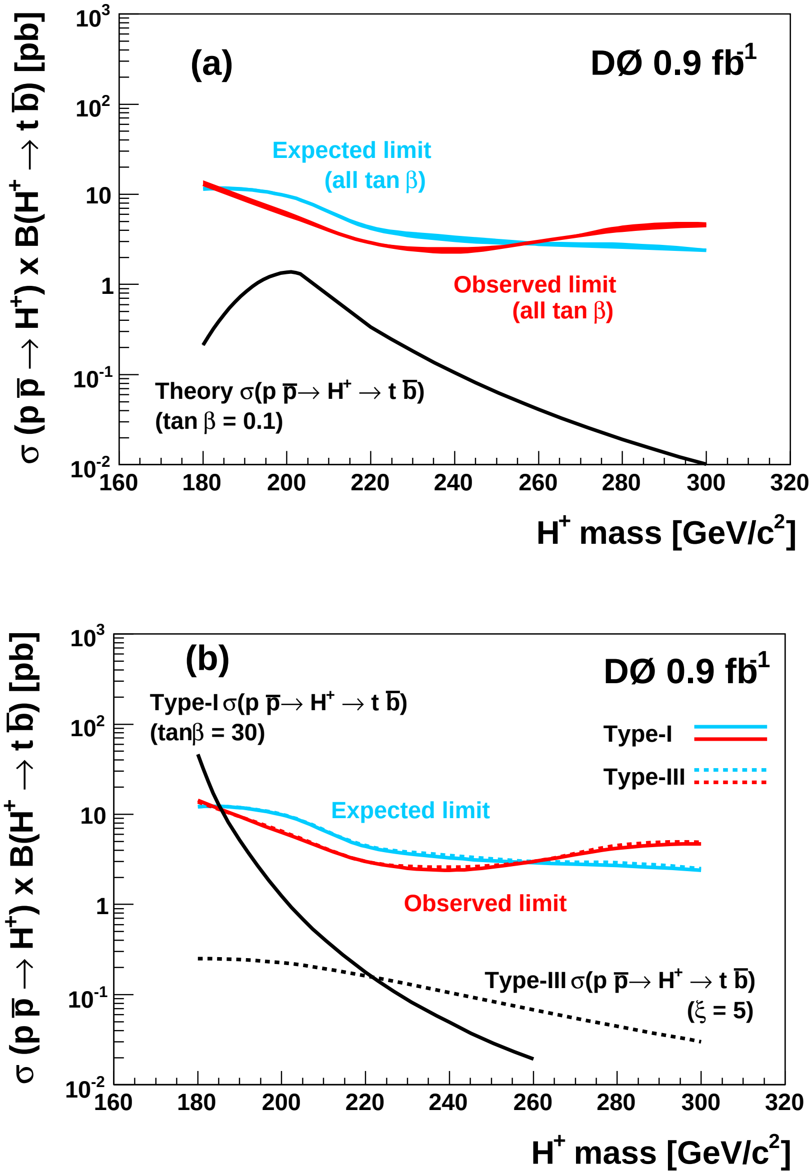

Figure 6–2: Observed and expected upper limits on the charged Higgs boson production cross-section times branching fraction at the 95% confidence level for different charged Higgs boson mass cases: (a) Type-II 2HDM, (b) Type I and III 2HDMs. The band on (a) represents the dependence on $\tan\beta$.

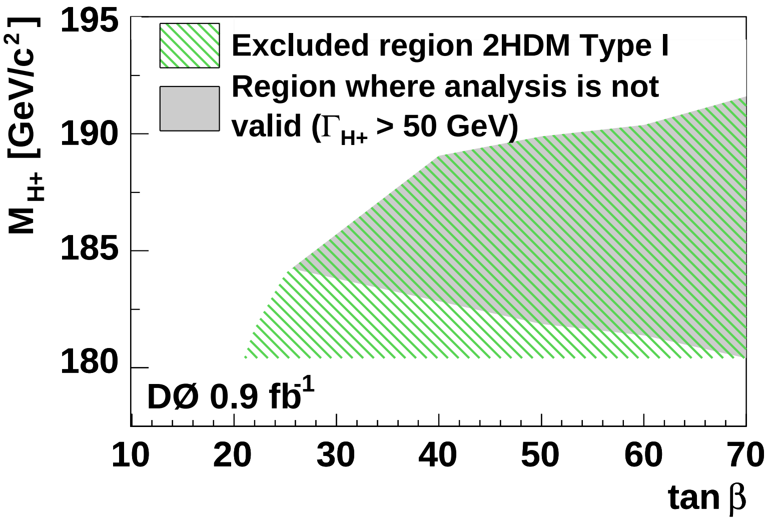

Figure 6–3: The 95% confidence level exclusion region in the $(M_{H^+}, \tan\beta)$ plane for the Type I 2HDM charged Higgs boson production. The exclusion region is represented by the green shaded area outside the grey area. The grey area represents parameter values where the charged Higgs width is larger than the experimental resolution. The analysis presented in this thesis is invalid for these parameter values. Values for upper limits on cross-section times branching ratio for charged Higgs boson production in the top and bottom quarks final state were used in order to extract the exclusion region. Systematic uncertainties that were taken into account in the upper limits calculation took into account shape changing effects on the invariant mass distributions hence the experimental resolution is not relevant to the points in $(M_{H^+}, \tan\beta)$ parameter space.

CHAPTER 7
Conclusion

The analysis described in this thesis represents the first search for charged Higgs boson production reconstructed in the top and bottom quark final state. Types I, II and III 2HDMs were investigated in the mass range $180 \leq M_{H^+} \leq 300$ GeV/c^2. No evidence for the production of charged Higgs bosons was found. Upper limits on charged Higgs boson production cross-sections were derived for Types I, II and III 2HDMs.

Upper limits on the charged Higgs boson production cross-section for the Type I 2HDM were translated into a 95% confidence level exclusion region in $(M_{H^+}, \tan\beta)$ parameter space. No region in $(M_{H^+}, \tan\beta)$ parameter space was excluded for the Type II 2HDM since the charged Higgs boson width was larger than the experimental resolution. For the Type III 2HDM, this analysis did not exclude charged Higgs boson production for values in (M_{H^+}, ξ) parameter space where the expected width is significantly smaller than the experimental resolution.

The sensitivity in a future DØ search for the production of charged Higgs bosons decaying to top and bottom quarks could benefit from the implementation of the following: (1) charged Higgs boson signal samples generated as a function of the total width, (2) optimised event selection for different charged Higgs boson masses and total widths, (3) the use of multivariate techniques to discriminate the charged

Higgs boson signal from the background and (4) an increase in the amount of data analysed.

Appendix A

Preselection Cuts

Preselection cuts were applied on data, background and charged Higgs boson signal samples. The cuts were developed for events in electron and muon analysis channels, where W^+ bosons decay to $e^+\nu$ and $\mu^+\nu$, respectively. Full preselection cut definitions are explained in Ref. [33] and summarised here.

Electron and Muon Channels

- One primary vertex, $|z_{\mathrm{PV}}| < 60$ cm, with three or more tracks attached
- Missing transverse energy within $15 < \not\!\!E_T < 200$ GeV.
- Two jet requirement: leading jet with $p_T > 25$ GeV/c and $|\eta| < 2.5$, and the second leading jet with $p_T > 20$ GeV/c and $|\eta| < 3.4$
- Fewer than three noise jets[1]
- Jet triangle cut that removes events with values in parameter space $|\Delta\phi(\text{leading jet}, \not\!\!E_T)|$ versus $\not\!\!E_T$ that are constrained by the functions $|\Delta\phi| = (0.0469\ \not\!\!E_T/\mathrm{GeV} + 1.5)$ radians and $|\Delta\phi| = 3.14$ radians.

Electron Channel

- Electron coming from the primary vertex $|\Delta z(e, \mathrm{PV})| < 1$ cm
- Only one tight electron with $E_T > 15$ GeV within $|\eta| < 1.1$
- No second loose electron with $E_T > 15$ GeV

---

[1] ”Noise jets” are defined as jets reconstructed by low energy or noisy calorimeter cells that give signal above threshold in a 3D isolated region [44].

- No tight muon with $p_T > 18$ GeV/c reconstructed within $|\eta| < 2.0$
- Triangle cut that removes events with values in parameter space $|\Delta\phi(e, \not\!\!E_T)|$ versus $\not\!\!E_T$ that are constrained by the functions:

  $|\Delta\phi| = (-0.05\ \not\!\!E_T/\text{GeV} + 2)$ radians and $|\Delta\phi| = 0$ radians

  $|\Delta\phi| = (-0.03\ \not\!\!E_T/\text{GeV} + 1.5)$ radians and $|\Delta\phi| = 0$ radians

  $|\Delta\phi| = (0.0475\ \not\!\!E_T/\text{GeV} + 1.14)$ radians and $|\Delta\phi| = 3.14$ radians

Muon Channel

- Muon coming from the primary vertex $|\Delta z(\mu, \text{PV})| < 1$ cm
- Only one tight muon with $p_T > 18$ GeV/c within $|\eta| < 2.0$
- No tight electron with $p_T > 15$ GeV/c reconstructed within $|\eta| < 2.5$
- Triangle cut that removes events with values in parameter space $|\Delta\phi(\mu, \not\!\!E_T)|$ versus $\not\!\!E_T$ that are constrained by the functions:

  $|\Delta\phi| = (-0.0138\ \not\!\!E_T/\text{GeV} + 1.1)$ radians and $|\Delta\phi| = 0$ radians

  $|\Delta\phi| = (-0.03\ \not\!\!E_T/\text{GeV} + 1.5)$ radians and $|\Delta\phi| = 0$ radians

  $|\Delta\phi| = (0.0213\ \not\!\!E_T/\text{GeV} + 0.64)$ radians and $|\Delta\phi| = 3.14$ radians

Misreconstructed track objects result in mismeasured transverse momentum. These cases, mainly in muon channel events [44], can result in too large missing transverse energies. A cut is therefore imposed to remove events with missing transverse energy $\not\!\!E_T > 200$ GeV.

Triangle cuts reject events containing misreconstructed objects that cause incorrect missing transverse energy measurements [44]. Such events include cases where a mismeasured or miscalibrated jet is assigned too high energy and generates a missing transverse energy contribution back-to-back with the jet. Triangle cuts also remove some of the events where a jet passes the electron identification requirements and gets misidentified as an electron with low transverse energy.

Appendix B

b Tagging

b tagging on Data and Multijet Samples

Jets in data events are required to be taggable before applying the *b* tagging algorithm [33]. The taggability procedure imposes jet quality requirements to reject badly reconstructed jets and to avoid unwanted detector effects. Events that pass the taggability criteria are processed by the neural network tagger. The neural network tagger incorporates input variables based on three other taggers. These taggers exploit known features of *b* jets to distinguish the *b* jets from other jets [43]. The average *b* tag efficiency on data is 47% for jets up to $|\eta| = 2.5$ and the average fake rate is 0.47% for central calorimeter jets [33].

b tagging on Monte Carlo Simulated Samples

Taggability requirements and the neural network tagger cannot be applied directly on Monte Carlo simulated samples since jets in Monte Carlo events have slightly different kinematics than jets in data.

An alternative taggability procedure is used on Monte Carlo simulated events. This procedure determines the jet taggability in Monte Carlo simulated events by using the average probability that a jet is taggable with, so called, taggability-rate functions. These functions were derived separately from electron and muon channel data and were defined as the ratio of the number of taggable jets in an event over the total number of good jets [33].

The average probability that a taggable jet passed the tagging algorithm was quantified by the tag-rate function [33] defined as the product of the taggability-rate function and the efficiency to identify b jets in data. Tag-rate functions were applied on jets in Monte Carlo events to estimate the number of tagged jets per event.

Appendix C

Statistical and Systematic Uncertainties

Table C-1 lists the relative systematic and statistical uncertainties considered in this analysis.

Table C-1: Summary of relative systematic and statistical uncertainties (in percent). Each column includes a range of systematic uncertainties associated with electron and muon channel samples. For the signal, the ranges of systematic uncertainties are relevant for all mass cases and for Types I, II and III 2HDMs. The normalisation method for W+jets and multijet samples is named "Matrix method." Tag-rate functions are given the acronym TRFs.

	H^+ signal		Background	
	1 b-tag	2 b-tag	1 b-tag	2 b-tag
Components for Normalisation				
Initial state parton contribution	10.0	10.0	—	—
Luminosity[a]	6.1	6.1	6.1	6.1
cross-section[a]	16	16	15.0 - 18.0	15.0 - 18.0
branching fraction[a]	1.0	1.0	1.0	1.0
Matrix method[b]	—	—	18.2 - 20.7	26.5 - 27.6
Primary vertex[a]	2.4 - 3.0	2.4 - 3.0	2.4 - 3.0	2.4 - 3.0
Lepton ID[a]	5.5 - 7.4	5.5 - 7.4	5.5 - 7.4	5.5 - 7.4
Jet ID[a]	1.5	1.5	1.5	1.5
Jet fragmentation[a]	5.0	5.0	5.0 - 7.0	5.0 - 7.0
Trigger[a]	3.0 - 6.0	3.0 - 6.0	3.0 - 6.0	3.0 - 6.0
Components for Normalisation and Shape				
Jet energy scale[a]	1.5 - 10.3	0.6 - 10.7	0.3 - 20.1	0.8 - 19.7
Flavour-dependent TRFs[c]	1.1 - 3.2	11.8 - 13.2	1.8 - 7.5	12.0 - 16.1
Statistics	0.4	0.7	0.4	1.2

[a] Does not apply for W+jets or multijets backgrounds

[b] Applies only for W+jets and multijets backgrounds

[c] Does not apply for multijets background

Appendix D

Constructing a Binned Likelihood Function

Upper limits on the charged Higgs boson production cross-section were derived using a Bayesian statistical approach [45]. Invariant mass distributions were used as the discriminating variable to construct a binned likelihood function. The likelihood function incorporated observed data and expected background counts and was used to derive the charged Higgs cross-section limits at the 95% confidence level.

Number of events in separate bins of the invariant mass distributions for data, background and charged Higgs boson signal samples were used to construct the likelihood function, $L(D|d)$. The symbol D represents the observed data count and d the expected sum of the signal and background event yields. The likelihood function is assumed to follow a Poisson distribution that defines the probability to observe the count D, given the expected count d. The event yield of the expected charged Higgs boson signal is expressed in terms of the cross-section (σ), signal acceptance ($\mathcal{A}$) and integrated luminosity ($\mathcal{L}$). The likelihood function was inverted using Bayes' theorem [46] to obtain the posterior probability density

$$P(\sigma, \mathcal{A}, \mathcal{L}, b|D) = \frac{L(D|\sigma, \mathcal{A}, \mathcal{L}, b)\pi(\sigma, \mathcal{A}, \mathcal{L}, b)}{\mathcal{N}}$$

where b represents the background event yield and the components are defined as follows:

- $P(\sigma, \mathcal{A}, \mathcal{L}, b|D)$ is the posterior probability density for observing the expected cross-section σ, given the observed count D.

- $L(D|\sigma, \mathcal{A}, \mathcal{L}, b)$ is the likelihood function which defines the probability of observing the count D, given the expected cross-section σ.
- $\pi(\sigma, \mathcal{A}, \mathcal{L}, b)$ is called the prior and defines the probability of observing the expected cross-section σ.
- $\mathcal{N}$ gives the overall normalisation such that $\int P(\sigma|D)d\sigma = 1$.

The posterior probability density $P(\sigma|D)$ to observe the charged Higgs boson cross-section σ is obtained by integration of the likelihood function and the prior with respect to the acceptance and the background event yields. The domain of the integral is constrained by variances of Gaussian functions where the means are defined as the acceptance and background event yields. The signal cross-section is assumed to be independent which allows for the factorisation of the prior, such that $\pi(\sigma, \mathcal{A}, \mathcal{L}, b) = \pi(\sigma)\pi(\mathcal{A}, \mathcal{L}, b)$, where the last factor is taken to be a Gaussian function. The prior for the signal cross-section is assumed to be constant and non-negative and is defined as $\pi(\sigma) = 1/\sigma_{max}$, when $0 < \sigma < \sigma_{max}$, and 0 otherwise. Cross-section values greater than the value σ_{max} results in negligible posterior probabilities. An upper limit on the production cross-section at the 95% confidence level is obtained by solving the equation

$$\int_0^{\sigma_{0.95}} P(\sigma|D)d\sigma = 0.95$$

Invariant mass distributions for data, background and charged Higgs boson samples were divided into 100 bins between 0 and 800 GeV. The binning allowed to exploit the discrimination power contained in the shapes of these distributions. A likelihood function was constructed for each separate bin. Since the bins were analysed as independent entities, the product of all 100 likelihoods times four analysis channels was used in the calculation of the posterior probability density. All systematic uncertainties and correlations were taken into account. The uncertainties were modelled by sampling acceptances and background event yields for the prior function from a Gaussian function. The mean of the Gaussian was defined by the nominal acceptance and background event yields. The width of the Gaussian was defined by acceptance and background event yields that were affected by a one standard deviation shift in the systematic uncertainty components.

References

[1] W.-M. Yao *et al.*, J. Phys. G: Nucl. Part. Phys. **33** (2006).

[2] D. J. Griffiths, *Introduction to Elementary Particles* (Wiley, New York, USA, 1987).

[3] F. Halzen and A. D. Martin, *Quarks & Leptons: An Introductory Course in Modern Particle Physics* (Wiley, New York, USA, 1984).

[4] M. E. Peskin and D. V. Schroeder, *An Introduction to Quantum Field Theory* (Westview Press, Reading, USA, 1995).

[5] J. F. Gunion, H. E. Haber, G. Kane, and S. Dawson, *The Higgs Hunter's Guide* (Addison Wesley, Reading, USA, 1990).

[6] M. Sher, Scalar–Mediated Flavor–Changing Neutral Currents, `arXiv:hep-ph/9809590` (1998).

[7] H. Logan, private communication (2007).

[8] C. Balázs, H.-J. He, and C.-P. Yuan, Phys. Rev. D **60**, 114001 (1999).

[9] H.-J. He and C.-P. Yuan, Phys. Rev. Lett. **83**, 1 (1999).

[10] E. Boos, V. Bunichev, L. Dudko, G. Kertzscher, C. Potter, and B. Vachon, A search for a heavy charged higgs boson reconstructed in the *tb* final state, DØ Note 5552 (2007).

[11] E. Boos *et al.*, Nucl. Instrum. Methods Phys. Res., Sect. A **534**, 250 (2004).

[12] A. Djouadi, J. Kalinowski, and M. Spira, HDECAY: a program for Higgs boson decays in the Standard Model and its supersymmetric extension, `arXiv:hep-ph/9704448` (1997).

[13] G. Abbiendi *et al.*, Eur. Phys. J. C **7**, 407 (1999).

[14] R. Barate *et al.*, Phys. Lett. B **543**, 1 (2002).

[15] J. Abdallah *et al.*, Phys. Lett. B **525**, 17 (2002).

[16] P. Achard *et al.*, Phys. Lett. B **575**, 208 (2003).

[17] B. Abbott *et al.*, Phys. Rev. Lett. **82**, 4975 (1999).

[18] V. Abazov *et al.*, Phys. Rev. Lett. **88**, 151803 (2002).

[19] A. Abulencia *et al.*, Phys. Rev. Lett. **96**, 042003 (2006).

[20] ALEPH, DELPHI, L3, and OPAL Collaborations (The LEP working group for Higgs boson searches), Searches for Higgs bosons: Preliminary combined results using LEP data collected at energies up to 202 GeV, CERN-EP-2000-055 (2000).

[21] ALEPH, DELPHI, L3, and OPAL Collaborations (The LEP working group for Higgs boson searches), Searches for Higgs bosons: Preliminary combined results using LEP data collected at energies up to 209 GeV, LHWG note 2001-05 (2001).

[22] M. Misiak *et al.*, Phys. Rev. Lett. **98**, 022002 (2007).

[23] Run II handbook, `http://www-bd.fnal.gov/lug/runii_handbook/runii_index.html`.

[24] V. Abazov *et al.*, Nucl. Instrum. Methods Phys. Res., Sect. A **565**, 463 (2006).

[25] S. Abachi *et al.*, Nucl. Instrum. Methods Phys. Res., Sect. A **338**, 185 (1994).

[26] C. W. Fabjan and F. Gianotti, Rev. Mod. Phys. **75**, 1243 (2003).

[27] V. Abazov *et al.*, Nucl. Instrum. Methods Phys. Res., Sect. A **552**, 372 (2005).

[28] T. Sjöstrand *et al.*, Comput. Phys. Commun. **135**, 238 (2001).

[29] R. Brun and F. Carminati, GEANT detector description and simulation tool, CERN Program Library Long Writeup W5013 (1993).

[30] D. Gillberg, Heavy Flavour Removal and Determination of Weighting Factors for ALPGEN W+jets Monte Carlo, DØ Note 5129 (2006).

[31] M. Mangano *et al.*, J. High Energy Phys. **0307**, 001 (2003).

[32] E. Boos *et al.*, Phys. Atom. Nucl. **534**, 1317 (2006).

[33] E. Aguiló *et al.* (DØ Single Top Group), Search for Single Top Quark Production in 1 fb^{-1} of Data, DØ Note 5285 (2007).

[34] A. Schwartzman and C. Tully, Primary Vertex Reconstruction by Means of Adaptive Vertex Fitting, DØ Note 4918 (2005).

[35] J. Hays *et al.*, Single Electron Efficiencies in p17 Data and Monte-Carlo using p18.05.00 d0correct, DØ Note 5105 (2006).

[36] J. Kozminski *et al.*, The Electron Likelihood in p14, DØ Note 4449 (2003).

[37] T. Gadfort *et al.*, Muon Identification Certification for p17 Data, DØ Note 5157 (2006).

[38] A. Harel, Jet ID Optimization, DØ Note 4919 (2006).

[39] J.-R. Vlimant *et al.*, Technical Description of the T42 Algorithm for Calorimeter Noise Suppression, DØ Note 4146 (2003).

[40] V. M. Abazov *et al.*, Phys. Rev. Lett. **98**, 18 (2007).

[41] DØ Common Samples Group webpage for p17 data, The trigger definitions that were used are under the *EMinclusive* and *MUinclusive* data skims, `http://www-d0.fnal.gov/Run2Physics/cs/skimming/fixPass2p170903.html`.

[42] E. Barberis *et al.*, The Matrix Method and its Error Calculation, DØ Note 4564 (2004).

[43] T. Scanlon, A Neural Network b-tagging Tool, DØNote 5213 (2007).

[44] The Single Top Working Group (DØ Collaboration), Search for Single Top Quark Production at DØ in Run II, DØ Note 4398 (2004).

[45] S. Jain, D. Kau, H. B. Prosper, R. Schwienhorst, and B. Vachon, Limits using a Bayesian approach in the package "top_statistics", DØ Note 5123 (2005).

[46] M. H. DeGroot and M. J. Schervish, *Probability and Statistics*, third edn. (Addison Wesley, Reading, USA, 2002).